

Supporting Information

Halogen Photoelimination from Dirhodium Phosphazane Complexes via Chloride-Bridged Intermediates

David C. Powers,^{a,b} Matthew B. Chambers^{a,b} Thomas S. Teets,^a Noémie
Elgrishi,^a Bryce, L. Anderson,^{a,b} and Daniel G. Nocera^{a,b,*}

^a *Department of Chemistry, Massachusetts Institute of Technology, 77 Massachusetts
Avenue, Cambridge, MA 02139-4307.* ^b *Department of Chemistry and Chemical
Biology, Harvard University, 12 Oxford Street, Cambridge, MA 02138-2902*

Email: dnocera@fas.harvard.edu

Table of Contents

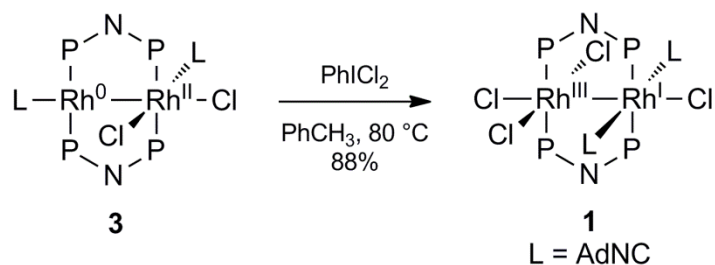
A. Materials and Methods	3
B. Synthesis and Characterization of New Complexes	3
B.1. Synthesis of Rh ₂ (tfepma) ₂ (AdNC) ₂ Cl ₄ (1)	3
B.2. Synthesis of Rh ₂ (tfepma) ₂ (μ- <i>p</i> -F-C ₆ H ₄ NC)Cl ₂ (6)	4
B.3. Synthesis of Rh ₂ (tfepma) ₂ (μ- <i>p</i> -MeO-C ₆ H ₄ NC)Cl ₂ (7)	4
B.4. Synthesis of Rh ₂ (tfepma) ₂ (<i>p</i> -F-C ₆ H ₄ NC)(μ-Cl)Cl ₃ (8)	5
B.5. Synthesis of Rh ₂ (tfepma) ₂ (<i>p</i> -MeO-C ₆ H ₄ NC)(μ-Cl)Cl ₃ (9)	5
C. NMR Data	6
D. X-Ray Data Analysis	15
D.1. Structural Data for Rh ₂ (I,III)(tfepma) ₂ (CNAd) ₂ Cl ₄ (1)	15
D.2. Structural Data for Rh ₂ (tfepma) ₂ (μ- <i>p</i> -F-C ₆ H ₄ NC)Cl ₂ (6)	17
D.3. Structural Data for Rh ₂ (tfepma) ₂ (μ- <i>p</i> -MeO-C ₆ H ₄ NC)Cl ₂ (7)	19
D.4. Structural Data for Rh ₂ (tfepma) ₂ (<i>p</i> -F-C ₆ H ₄ NC)(μ-Cl)Cl ₃ (8)	21
D.5. Structural Data for Rh ₂ (tfepma) ₂ (<i>p</i> -MeO-C ₆ H ₄ NC)(μ-Cl)Cl ₃ (9)	23
E. Steady-State Photolysis Data	25
E.1. Photolysis of 1 and 2	25
E.2. Spectral Fitting to Obtain Concentration Plots	30
E.3. Determination of Quantum Yields	33
E.4. Steady-State Photolysis of Rh ₂ (tfepma) ₂ (<i>p</i> -F-C ₆ H ₄ NC)(μ-Cl)Cl ₃ (8)	35
E.5. Thermolysis of Rh ₂ (tfepma) ₂ (<i>p</i> -F-C ₆ H ₄ NC)(μ-Cl)Cl ₃ (8)	36
F. Time-Resolved Photochemical Experiments	36
F.1. General Considerations	36
F.2. Comparison of Absorption Spectra of Transient Intermediate with Chloride-Bridged Structures	42
G. Computational Analysis	43
G.1. Computational Methods	43
G.2. Cartesian Coordinates of Computed Structures	45
G.3. Comparison of Computed Structures and X-ray Structures	50
H. Time-Dependant DFT Analysis	51
H.1. Excited State Calculation of Rh ₂ [I,III] Structure A	51
H.2. Excited State Calculation of Rh ₂ [I,III] Structure B	55
H.3. Excited State Calculation of Chloride-Bridged Dirhodium Structure C	59
H.4. Full Citation for Reference 13	60

A. Materials and Methods

All reactions were carried out in an N₂-filled glovebox. Anhydrous solvents were obtained by filtration through drying columns.¹ NMR spectra were recorded at the MIT Department of Chemistry Instrument Facility (DCIF) on a Varian Mercury 300 MHz spectrometer, operating at 300 MHz for ¹H acquisitions and at 121.5 MHz for ³¹P acquisitions. NMR chemical shifts are reported in ppm with the residual solvent resonance as internal standard. ³¹P NMR chemical shifts were referenced to an external 85% D₃PO₄ standard. IR spectra were recorded on a Perkin Elmer Spectrum 400 FT-IR/FT-FIR spectrometer outfitted with a Pike Technologies GladiATR attenuated total reflectance accessory with a monolithic diamond stage and pressure clamp. Samples were suspended in Nujol® for all IR measurements. UV-vis spectra were recorded at 293 K in quartz cuvettes on a Spectral Instruments 400 series diode array and were blanked against the appropriate solvent. Photochemical reactions were performed using a 1000 W high-pressure Hg/Xe arc lamp (Oriol) and the beam was passed through a water-jacketed filter holder containing the appropriate long-pass filter, an iris and a collimating lens. [Rh(cod)Cl]₂ was obtained from Strem Chemicals and used without purification. Phosphazane ligand tfepma² and AdNC³ were prepared as described in the literature. Complexes **2** and **3** were prepared according to procedures we have previously reported.⁴

B. Synthesis and Characterization of New Complexes

B.1. Synthesis of Rh₂(tfepma)₂(AdNC)₂Cl₄ (**1**)



To a saturated solution of Rh₂[0,II] complex **3** (50.0 mg, 3.18 × 10⁻⁵ mol, 1.00 equiv) in PhCH₃ was added PhI₂Cl₂ (17.5 mg, 6.36 × 10⁻⁵ mol, 2.00 equiv) as a solid. The reaction solution was heated to 80 °C for 10 h, during which time a green solid precipitated. The reaction mixture was cooled to -20 °C for 20 min, at which time the green solid was collected, washed with pentane, and dried in vacuo to afford 46 mg of the title complex

¹ Pangborn, A. B.; Giardello, M. A.; Grubbs, R. H.; Rosen, R. K.; Timmers, F. J. *Organometallics* **1996**, *15*, 1518–1520.

² Teets, T. S.; Cook, T. R.; Nocera, D. G. *Inorg. Synth.* **2010**, *35*, 164.

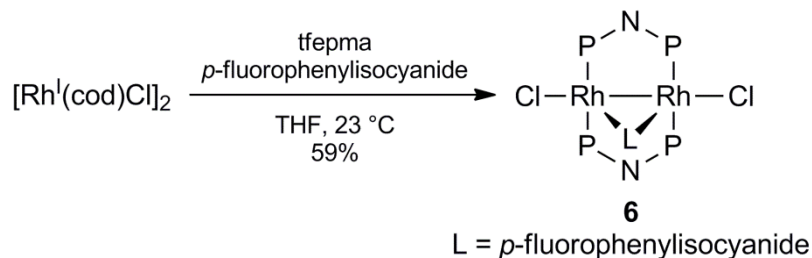
³ Sasaki, T.; Nakanishi, A.; Ohno, M. *J. Org. Chem.* **1981**, *46*, 5445.

⁴ Elgrishi, N.; Teets, T. S.; Chambers, M. B.; Nocera, D. G. *Chem. Commun.* **2012**, 9474.

(88% yield).

^1H NMR (300 MHz, THF- d_8) δ (ppm): 5.21–4.73 (m, 16H), 3.10 (pseudoquintet, $J = 4.1$ Hz, 6H), 2.11 (s, 18H), 1.71 (s, 12H). $^{31}\text{P}\{^1\text{H}$ NMR (121.5 MHz, THF- d_8) δ (ppm): 113.8 (m, 4P). IR: $\nu_{\text{CN}} = 2211$ cm^{-1} . Combustion Anal. Calc. C, 29.22; H, 3.19; N, 3.42; Found: C, 29.08; H, 3.21; N, 3.12. Crystals suitable for single-crystal diffraction analysis were obtained from a PhCH_3 solution and details appear in the Section D.1.

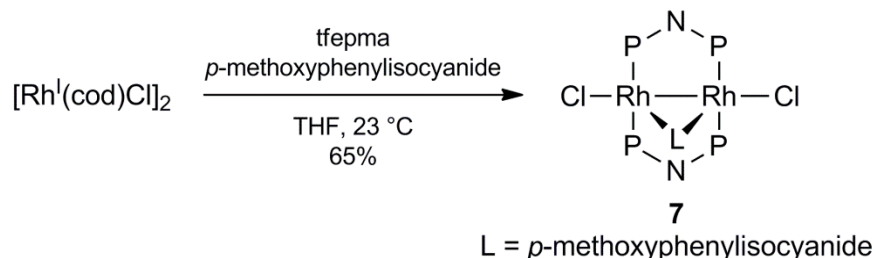
B.2. Synthesis of $\text{Rh}_2(\text{tfepma})_2(\mu\text{-}p\text{-F-C}_6\text{H}_4\text{NC})\text{Cl}_2$ (6)



To a solution of $[\text{Rh}(\text{cod})\text{Cl}]_2$ (33.0 mg, 6.70×10^{-5} mol, 1.00 equiv) in THF (4.0 mL), tfepma (65.3 mg, 1.34×10^{-4} mol, 2.00 equiv) and *p*-fluorophenylisocyanide (16.3 mg, 1.34×10^{-4} mol, 2.00 equiv) was added sequentially. The dark red reaction solution was stirred at 23 °C for 4 h. Solvent was removed in vacuo and the residue was taken up in THF (1 mL) and hexanes (10 mL). The supernatant was removed and the solid residue was dried in vacuo to afford 59 mg of the title complex (59% yield) as an orange solid.

^1H NMR (300 MHz, CD_2Cl_2) δ (ppm): 7.30 (dd, $J = 9.0$ Hz, $J = 4.9$ Hz, 2H), 7.05 (dd, $J = 8.3$ Hz, $J = 8.3$ Hz, 2H), 4.72–4.55 (m, 16H), 2.79 (pseudoquintet, $J = 3.5$ Hz, 6H). ^{31}P NMR (121.5 MHz, CD_2Cl_2) δ (ppm): 130.8 (m, 4P). IR: $\nu_{\text{CN}} = 1736$ cm^{-1} . Crystals suitable for single-crystal diffraction analysis were obtained from a PhCH_3 solution and details appear in the Section D.2.

B.3. Synthesis of $\text{Rh}_2(\text{tfepma})_2(\mu\text{-}p\text{-MeO-C}_6\text{H}_4\text{NC})\text{Cl}_2$ (7)

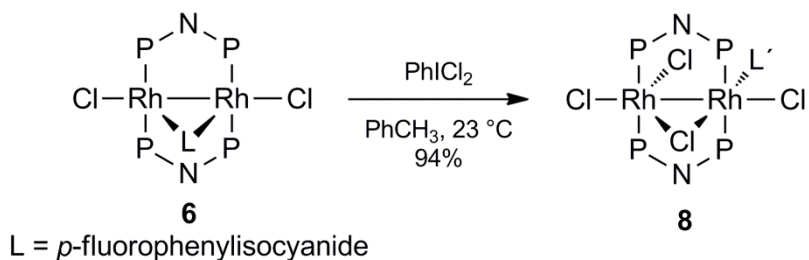


To a solution of $[\text{Rh}(\text{cod})\text{Cl}]_2$ (163 mg, 3.31×10^{-4} mol, 1.00 equiv) in THF (5.0 mL), tfepma (322 mg, 6.61×10^{-4} mol, 2.00 equiv) and *p*-methoxyphenylisocyanide (88.7 mg, 6.61×10^{-4} mol, 2.00 equiv) was added sequentially. The reaction solution was stirred at 23 °C for 4 h. Solvent was removed in vacuo and the residue was taken up in THF (2 mL) and hexanes (15

mL). The supernatant was removed and the solid residue was dried in vacuo to afford 298 mg of the title complex (65% yield).

^1H NMR (300 MHz, CD_2Cl_2) δ (ppm): 7.26 (d, $J = 9.0$ Hz, 2H), 6.85 (d, $J = 9.0$ Hz, 2H), 4.72–4.50 (m, 16H), 2.76 (pseudoquintet, $J = 3.5$ Hz, 6H). ^{31}P NMR (121.5 MHz, THF- d_8) δ (ppm): 132.2 (m, 4P). IR: $\nu_{\text{CN}} = 1783$ cm^{-1} . Crystals suitable for single-crystal diffraction analysis were obtained from a PhCH_3 solution and details appear in the Section D.3.

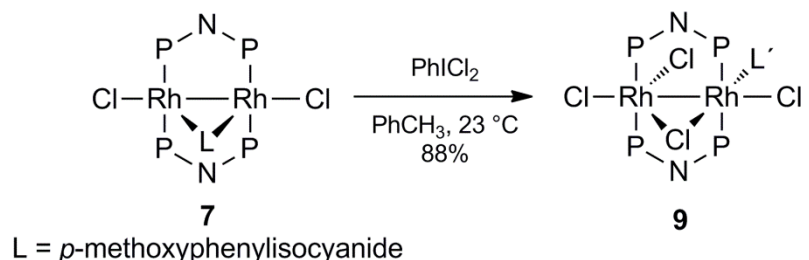
B.4. Synthesis of $\text{Rh}_2(\text{tfepma})_2(\mu\text{-}p\text{-F-C}_6\text{H}_4\text{NC})(\mu\text{-Cl})\text{Cl}_3$ (**8**)



To a solution of $\text{Rh}_2(\text{tfepma})_2(\mu\text{-}p\text{-F-C}_6\text{H}_4\text{NC})\text{Cl}_2$ (**6**) (127.0 mg, 9.25×10^{-5} mol, 1.00 equiv) in PhCH_3 at 23 °C was added PhICl_2 (26.7 mg, 9.71×10^{-5} mol, 1.05 equiv) as a solid in one portion. The color of the reaction mixture turned from orange to dark red. After stirring for 2 h at 23 °C, solvent was removed in vacuo and the residue was taken up in PhCH_3 (1 mL) and cooled to -30 °C for one hour. The supernatant was removed and the solid residue was dried in vacuo to afford 125 mg of the title complex (94% yield) as a dark orange solid.

^1H NMR (300 MHz, CD_2Cl_2) δ (ppm): 7.48 (dd, $J = 9.2$ Hz, $J = 4.6$ Hz, 2H), 7.16 (dd, $J = 8.2$ Hz, $J = 8.2$ Hz, 2H), 4.92–4.60 (m, 12H), 4.56–4.44 (m, 2H), 4.38–4.28 (m, 2H), 3.02 (pseudoquintet, $J = 3.8$ Hz, 6H). ^{31}P NMR (121.5 MHz, CD_2Cl_2) δ (ppm): 119.5–113.1 (m, 4P). ^{19}F NMR (275 MHz, CD_2Cl_2) δ (ppm): -73.7 (m, 24F), -105.0 (m, 24F). IR: $\nu_{\text{CN}} = 2181$ cm^{-1} . Crystals suitable for single-crystal diffraction analysis were obtained from a PhCH_3 solution; details appear in the Section D.4.

B.5. Synthesis of $\text{Rh}_2(\text{tfepma})_2(\mu\text{-}p\text{-MeO-C}_6\text{H}_4\text{NC})(\mu\text{-Cl})\text{Cl}_3$ (**9**)



To a solution of $\text{Rh}_2(\text{tfepma})_2(\mu\text{-}p\text{-MeO-C}_6\text{H}_4\text{NC})\text{Cl}_2$ (**7**) (88.0 mg, 6.35×10^{-5} mol, 1.00 equiv) in PhCH_3 (2 mL) at 23 °C was added PhICl_2 (19.2 mg, 6.98×10^{-5} mol, 1.10 equiv) as a solid in one portion. The color of the reaction mixture turned from orange to dark red.

After stirring for 2 h at 23 °C, solvent was removed in vacuo and the residue was taken up in PhCH₃ (0.7 mL) and cooled to -30 °C for one hour. The supernatant was removed and the solid residue was dried in vacuo to afford 81 mg of the title complex (88% yield) as a red-orange solid.

¹H NMR (300 MHz, CD₂Cl₂) δ (ppm): 7.41 (d, *J* = 9.0 Hz, 2H), 6.93 (d, *J* = 9.1 Hz, 2H), 4.94–4.64 (m, 12H), 4.54–4.44 (m, 2H), 4.40–4.30 (m, 2H), 3.85 (s, 3H), 3.03 (pseudoquintet, *J* = 3.5 Hz, 6H). ³¹P NMR (121.5 MHz, THF-*d*₈) δ (ppm): 119.8–113.4 (m, 4P). IR: ν_{CN} = 2189 cm⁻¹. Crystals suitable for single-crystal diffraction analysis were obtained from a PhCH₃ solution and details appear in Section D.5.

C. NMR Data

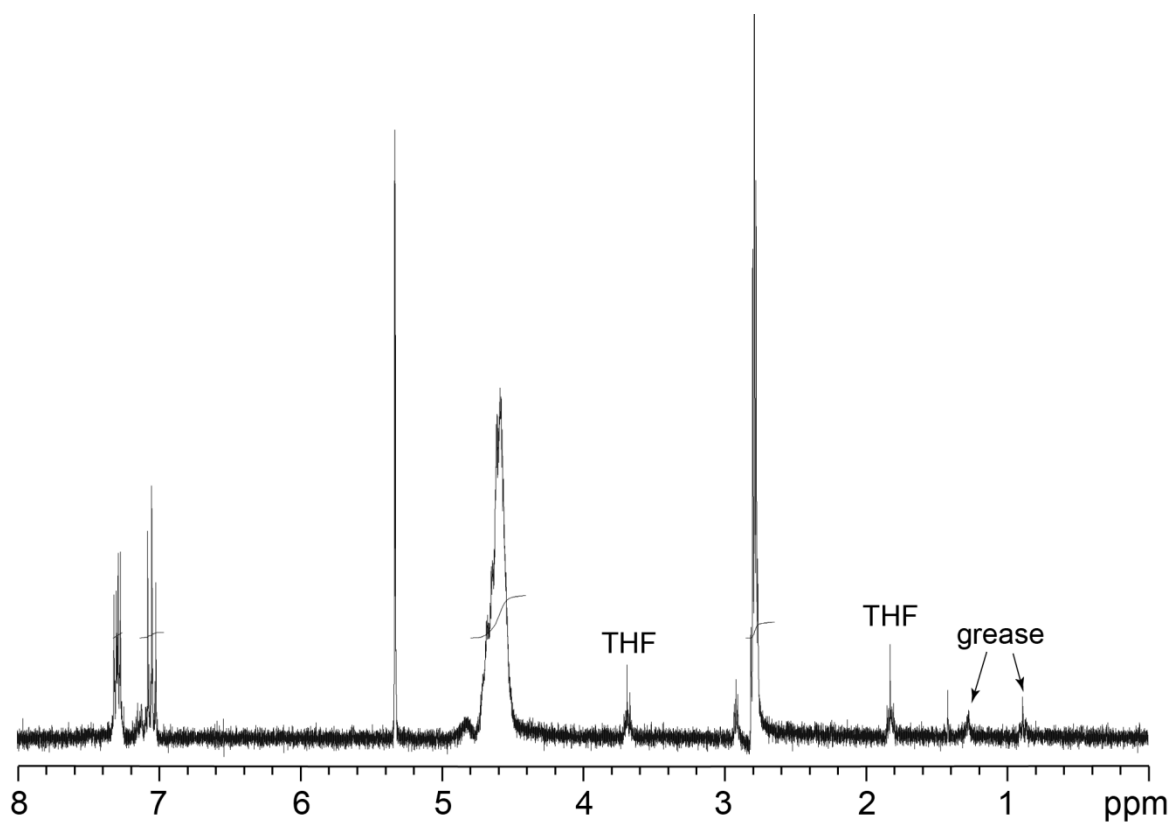


Figure S1. ¹H NMR spectrum of complex 6 recorded in CD₂Cl₂ at 23 °C.

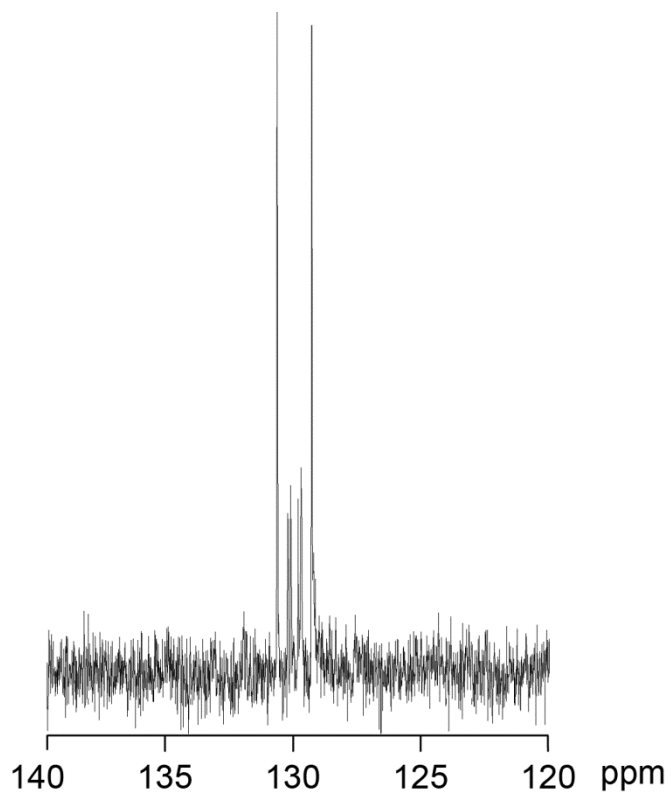


Figure S2. ^{31}P NMR spectrum of complex **6** recorded in CD_2Cl_2 at 23 °C.

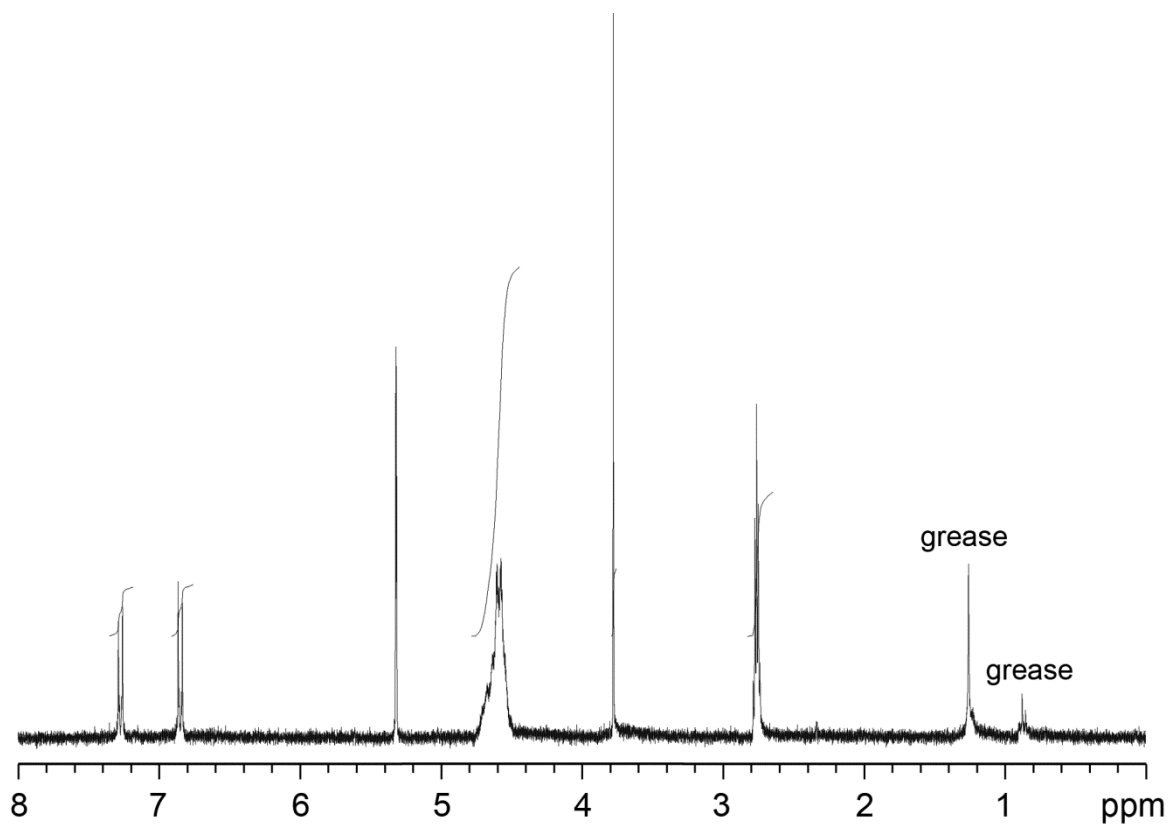


Figure S3. ^{19}F NMR spectrum of complex **7** recorded in CD_2Cl_2 at 23 °C.

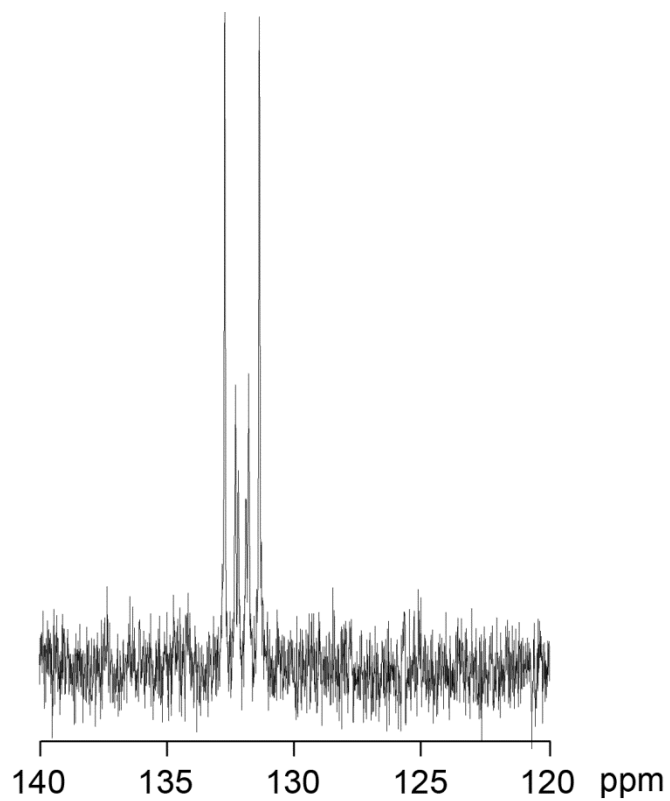


Figure S4. ^{19}F NMR spectrum of complex **7** recorded in CD_2Cl_2 at 23 °C.

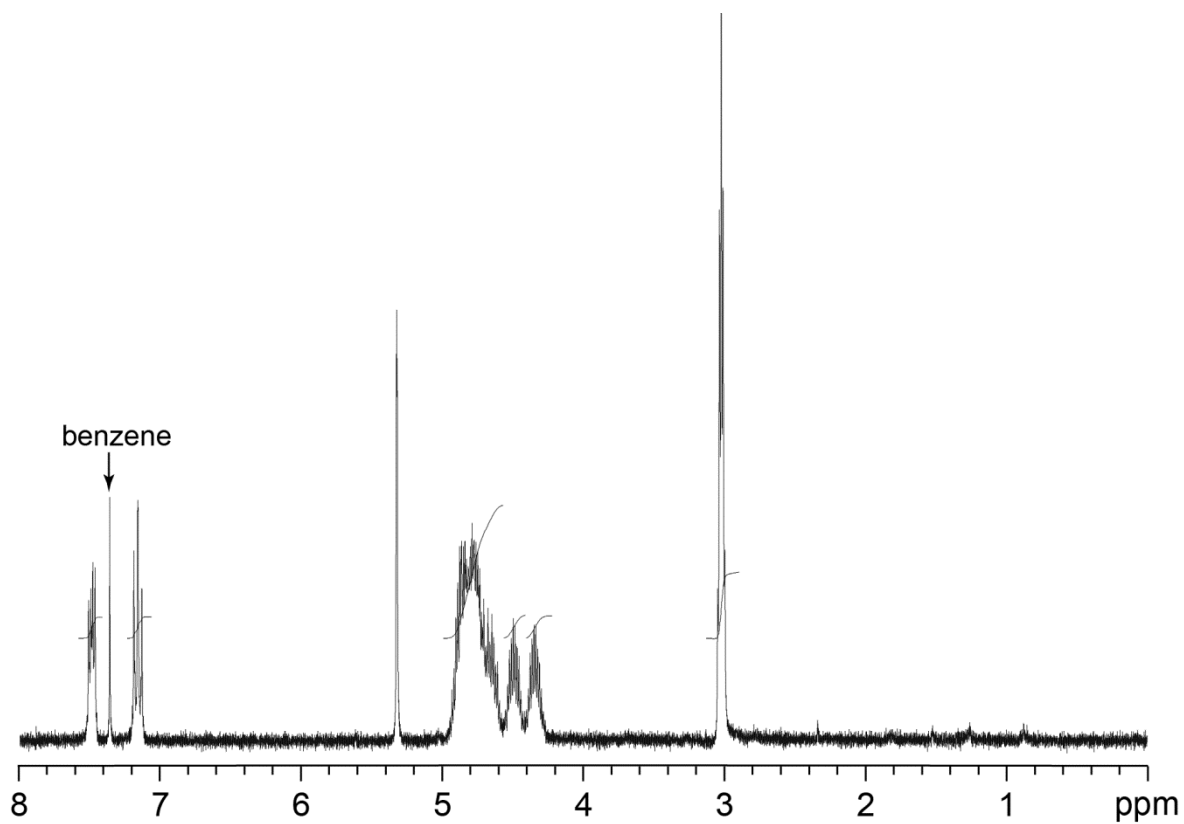


Figure S5. ¹H NMR spectrum of complex **8** recorded in CD₂Cl₂ at 23 °C.

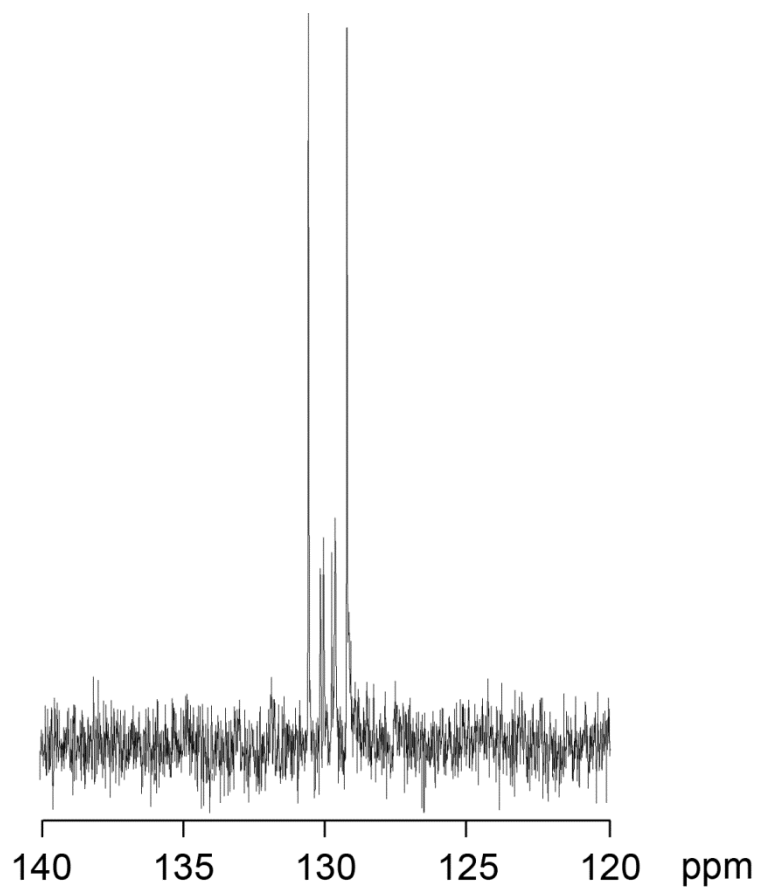


Figure S6. ^{31}P NMR spectrum of complex **8** recorded in CD_2Cl_2 at 23 °C.

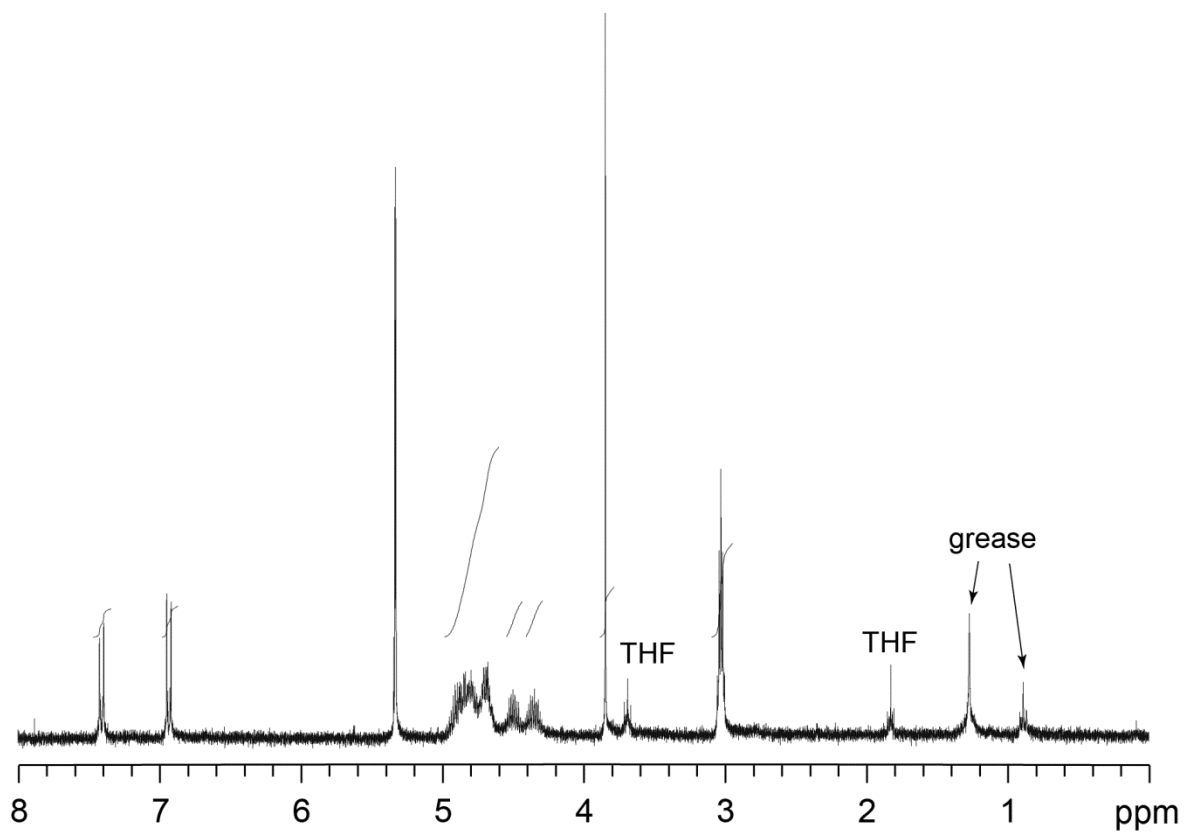


Figure S7. ¹H NMR spectrum of complex **9** recorded in CD₂Cl₂ at 23 °C.

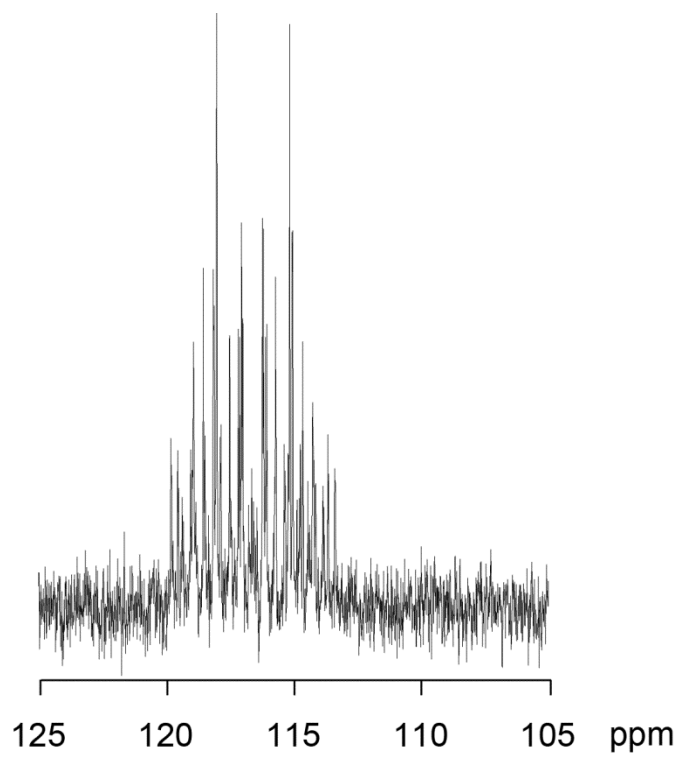


Figure S8. ^{31}P NMR spectrum of complex **9** recorded in CD_2Cl_2 at 23 °C.

D. X-Ray Data Analysis

D.1. Structural Data for $\text{Rh}_2(\text{I,III})(\text{tfepma})_2(\text{CNAd})_2\text{Cl}_4$ (**1**)

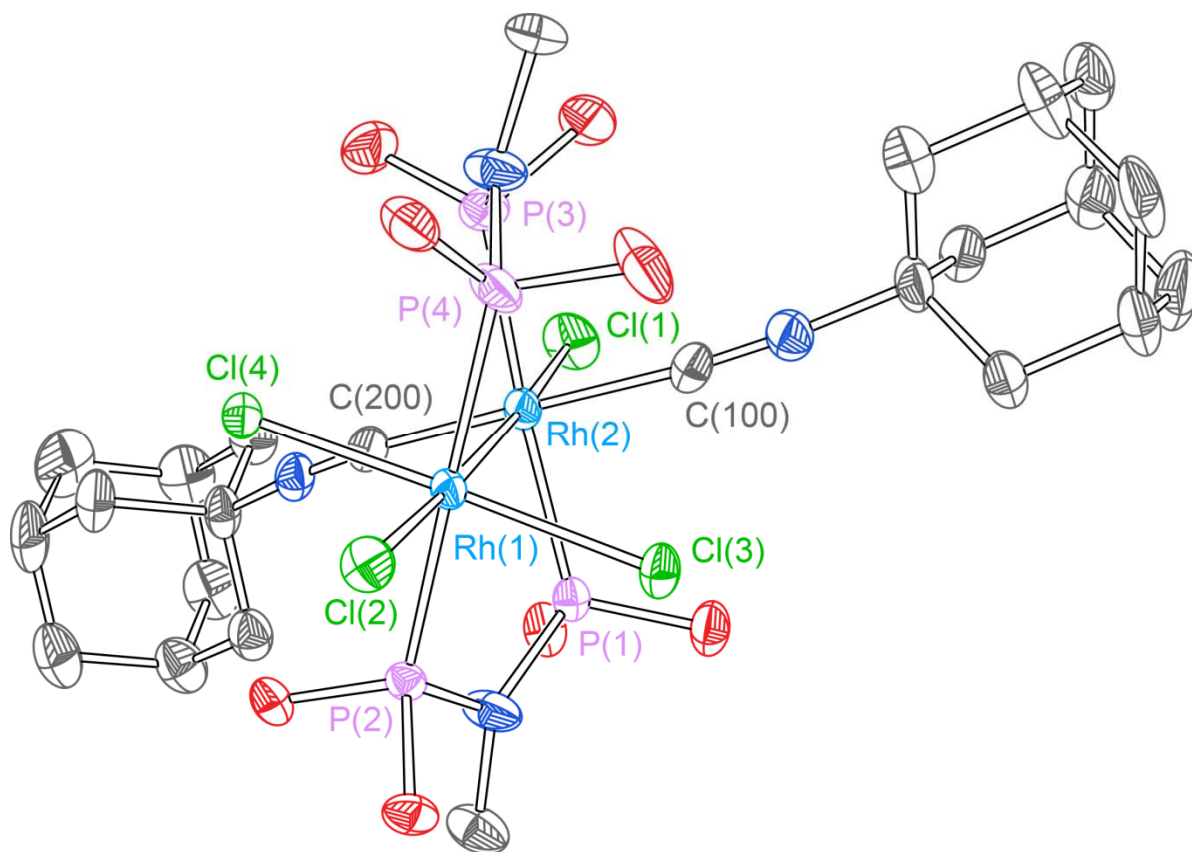


Figure S9. Thermal ellipsoid plot of $\text{Rh}_2[\text{I,III}]$ complex **1** drawn at the 50% probability level. The $-\text{CH}_2\text{CF}_3$ groups and hydrogen atoms are omitted for clarity.

Table S1. X-ray experimental details for Rh₂(I,III)(tfepma)₂(CNAd)₂Cl₄ (**1**)

Crystal Data

Chemical formula	C ₄₀ H ₅₂ Cl ₄ F ₂₄ N ₃ O ₈ P ₄ Rh ₂
Fw, g/mol	1644.35
Crystal system, space group	Monoclinic, <i>P</i> 2 ₁ / <i>n</i>
Temperature (K)	100
<i>a</i> , <i>b</i> , <i>c</i> (Å)	12.7242 (5), 20.3878 (8), 23.2389 (9)
<i>b</i> (°)	97.497 (1)
<i>V</i> (Å ³)	5977.1 (4)
<i>Z</i>	4
Radiation type	Mo <i>K</i> α
μ (mm ⁻¹)	0.95
Crystal size (mm)	0.40 × 0.40 × 0.20

Data collection

Diffractometer	Bruker APEX-II CCD
Absorption correction	Empirical (using intensity meas.) <i>SADABS</i>
<i>T</i> _{min} , <i>T</i> _{max}	0.702, 0.832
No. of measured, independent and observed [<i>I</i> > 2σ(<i>I</i>)] reflections	135954, 17477, 12674
<i>R</i> _{int}	0.063
(sin θ/λ) _{max} (Å ⁻¹)	0.704

Refinement

<i>R</i> [<i>F</i> ² > 2σ(<i>F</i> ²)], <i>wR</i> (<i>F</i> ²), <i>S</i>	0.048, 0.123, 1.01
No. of reflections	17477
No. of parameters	1024
No. of restraints	184
H-atom treatment	H-atom parameters constrained $w = 1/[\sigma^2(F_o^2) + (0.0405P)^2 + 19.7337P]$ where $P = (F_o^2 + 2F_c^2)/3$
Δ _{max} , Δ _{min} (e Å ⁻³)	1.93, -1.70

D.2. Structural Data for $\text{Rh}_2(\text{tfepma})_2(\mu\text{-}p\text{-F-C}_6\text{H}_4\text{NC})\text{Cl}_2$ (**6**)

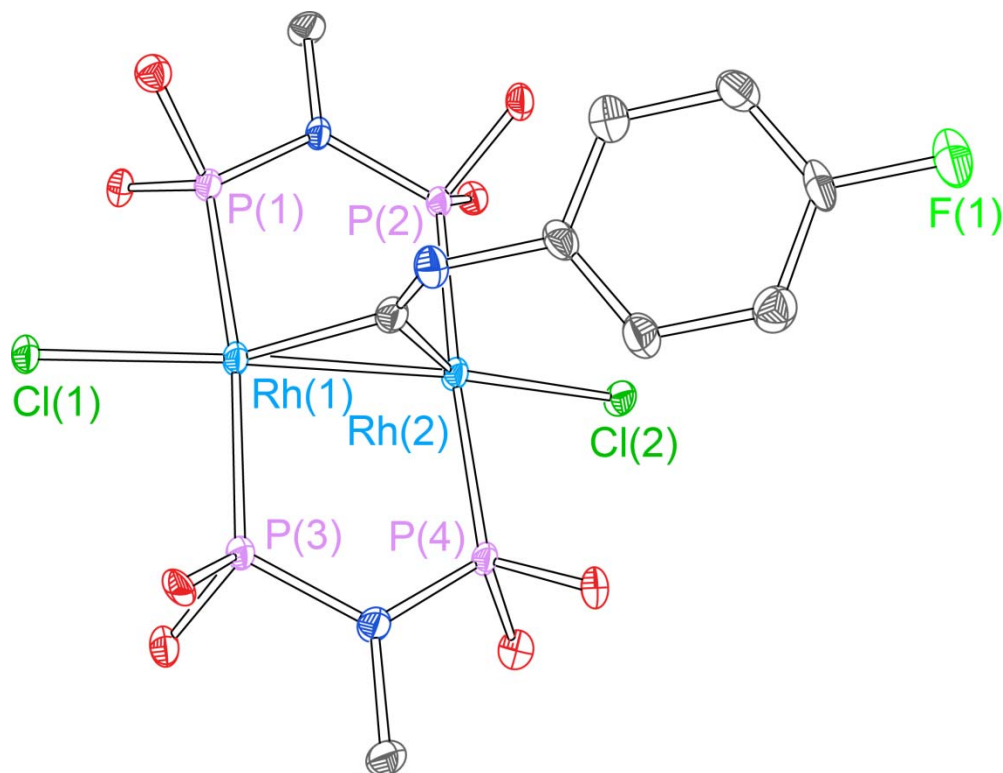


Figure S10. Thermal ellipsoid plot of **6** drawn at the 50% probability level. The $-\text{CH}_2\text{CF}_3$ groups and hydrogen atoms are omitted for clarity.

Table S2. X-ray experimental details for $\text{Rh}_2(\text{tfepma})_2(\mu\text{-}p\text{-F-C}_6\text{H}_4\text{NC})\text{Cl}_2$ (**6**)

Crystal data

Chemical formula	$\text{C}_{25}\text{H}_{26}\text{Cl}_2\text{F}_{25}\text{N}_3\text{O}_8\text{P}_4\text{Rh}_2$
Fw, g/mol	1372.09
Crystal system, space group	Triclinic, <i>P1</i>
Temperature (K)	100
<i>a</i> , <i>b</i> , <i>c</i> (Å)	10.1595 (9), 10.386 (1), 12.0283 (11)
α , β , γ (°)	73.962 (2), 69.049 (1), 71.477 (2)
<i>V</i> (Å ³)	1104.74 (18)
<i>Z</i>	1
Radiation type	Mo <i>K</i> α
μ (mm ⁻¹)	1.17
Crystal size (mm)	0.20 × 0.10 × 0.10

Data collection

Diffractometer	Bruker <i>APEX-II</i> CCD diffractometer
Absorption correction	Multi-scan <i>SADABS</i>
<i>T</i> _{min} , <i>T</i> _{max}	0.800, 0.892
No. of measured, independent and observed [<i>I</i> > 2σ(<i>I</i>)] reflections	25891, 12490, 11183
<i>R</i> _{int}	0.036
(sin θ/λ) _{max} (Å ⁻¹)	0.715

Refinement

$R[F^2 > 2\sigma(F^2)]$, $wR(F^2)$, <i>S</i>	0.037, 0.085, 1.03
No. of reflections	12490
No. of parameters	625
No. of restraints	3
H-atom treatment	H-atom parameters constrained
Δ_{max} , Δ_{min} (e Å ⁻³)	2.22, -0.80
Absolute structure	Flack, H. D. <i>Acta Cryst.</i> 1983 , A39, 876-881
Flack parameter	0.676 (17)

D.3. Structural Data for $\text{Rh}_2(\text{tfepma})_2(\mu\text{-}p\text{-MeO-C}_6\text{H}_4\text{NC})\text{Cl}_2$ (**7**)

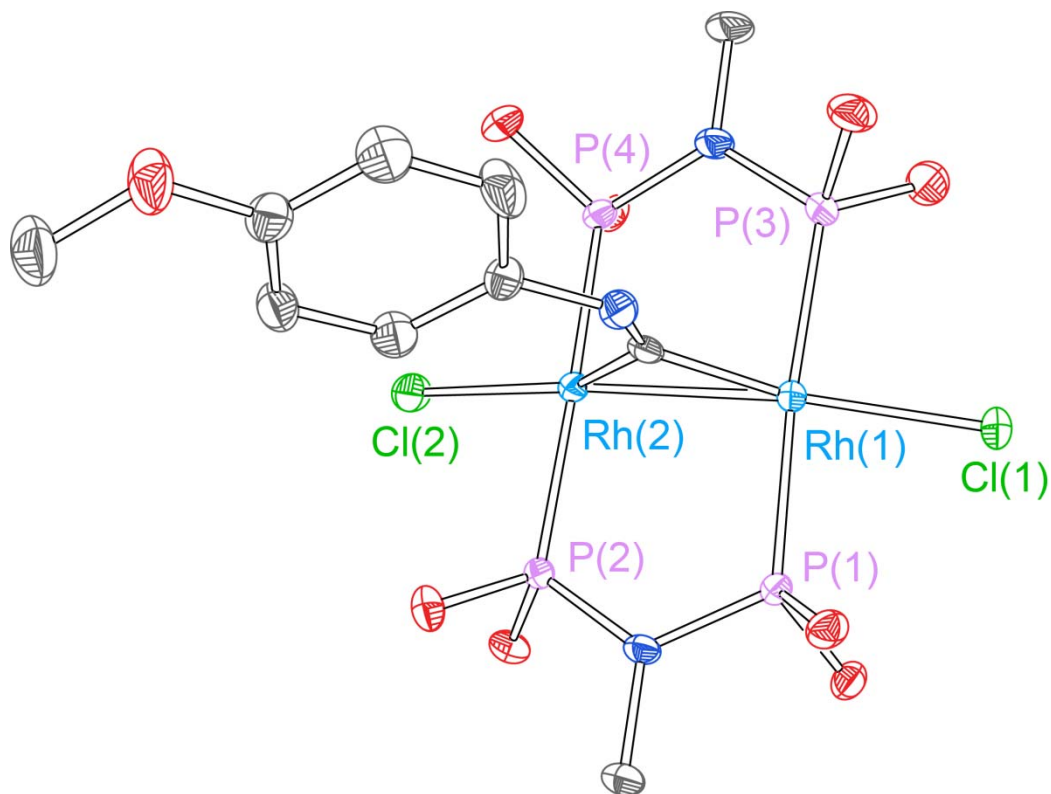


Figure S11. Thermal ellipsoid plot of **7** drawn at the 50% probability level. The -CH₂CF₃ groups and hydrogen atoms are omitted for clarity.

Table S3. X-ray experimental details for $\text{Rh}_2(\text{tfepma})_2(\mu\text{-}p\text{-MeO-C}_6\text{H}_4\text{NC})\text{Cl}_2$ (**7**)

Crystal data

Chemical formula	$\text{C}_{26}\text{H}_{29}\text{Cl}_2\text{F}_{24}\text{N}_3\text{O}_9\text{P}_4\text{Rh}_2$
Fw, g/mol	1384.12
Crystal system, space group	Monoclinic, $P2_1/c$
Temperature (K)	100
a, b, c (Å)	12.0403 (8), 19.3984 (13), 20.6248 (14)
β (°)	106.961 (1)
V (Å ³)	4607.6 (5)
Z	4
Radiation type	Mo $K\alpha$
μ (mm ⁻¹)	1.12
Crystal size (mm)	0.25 × 0.10 × 0.10

Data collection

Diffractometer	Bruker APEX-II CCD
Absorption correction	Multi-scan SADABS
T_{\min}, T_{\max}	0.767, 0.896
No. of measured, independent and observed [$I > 2\sigma(I)$] reflections	79113, 8770, 6365
R_{int}	0.089
$(\sin \theta/\lambda)_{\text{max}}$ (Å ⁻¹)	0.610

Refinement

$R[F^2 > 2\sigma(F^2)], wR(F^2), S$	0.040, 0.101, 1.03
No. of reflections	8770
No. of parameters	745
No. of restraints	1019
H-atom treatment	H-atom parameters constrained $w = 1/[\sigma^2(F_o^2) + (0.0363P)^2 + 14.3592P]$ where $P = (F_o^2 + 2F_c^2)/3$
$\Delta_{\text{max}}, \Delta_{\text{min}}$ (e Å ⁻³)	1.00, -0.64

D.4. Structural Data for $\text{Rh}_2(\text{tfepma})_2(p\text{-F-C}_6\text{H}_4\text{NC})(\mu\text{-Cl})\text{Cl}_3$ (**8**)

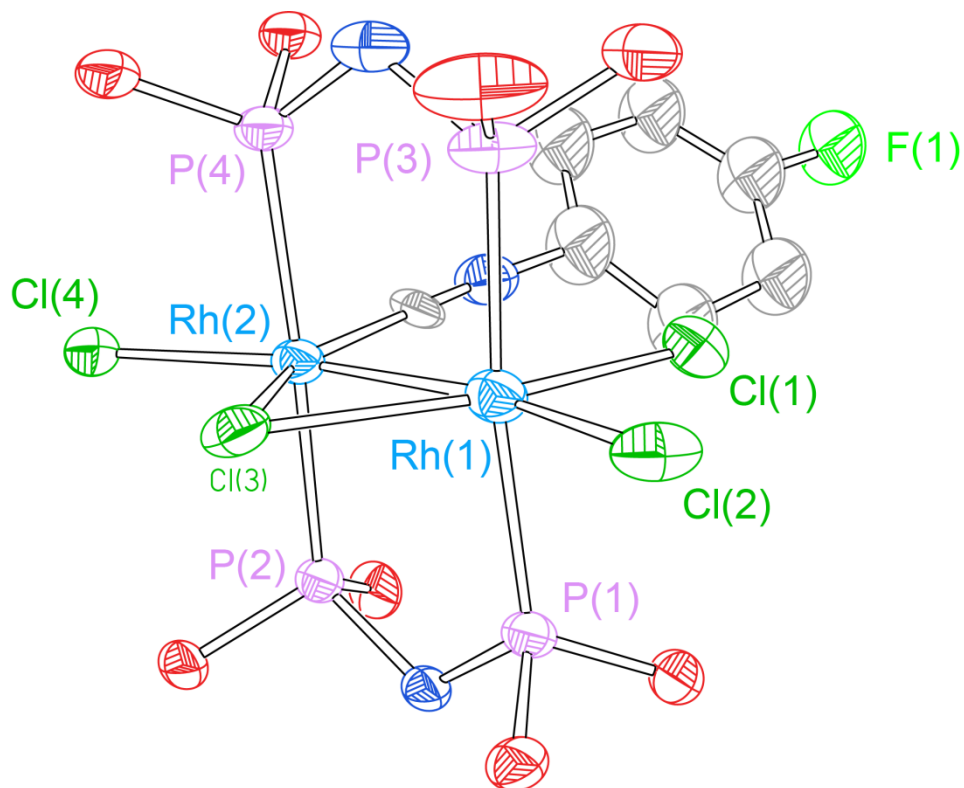


Figure S12. Thermal ellipsoid plot of **8** drawn at the 50% probability level. The $-\text{CH}_2\text{CF}_3$ groups and hydrogen atoms are omitted for clarity. The Squeeze function of PLATON was used to remove a highly disordered toluene solvent molecule during structure refinement of **8**.

Table S4. X-ray experimental details for $\text{Rh}_2(\text{tfepma})_2(p\text{-F-C}_6\text{H}_4\text{NC})(\mu\text{-Cl})\text{Cl}_3$ (**8**)

Crystal data

Chemical formula	$\text{C}_{25}\text{H}_{26}\text{Cl}_4\text{F}_{25}\text{N}_3\text{O}_8\text{P}_4\text{Rh}_2$
Fw, g/mol	1442.99
Crystal system, space group	Monoclinic, $P2_1/c$
Temperature (K)	100
a, b, c (Å)	12.2025 (13), 21.385 (2), 20.398 (2)
α, β, γ (°)	90, 98.351 (2), 90
V (Å ³)	5266.4 (10)
Z	4
Radiation type	Mo $K\alpha$
μ (mm ⁻¹)	1.08
Crystal size (mm)	0.10 × 0.10 × 0.10

Data collection

Absorption correction	Multi-scan
T_{\min}, T_{\max}	0.900, 0.900
No. of measured, independent and observed [$I > 2\sigma(I)$] reflections	10766, 10766, 8406
R_{int}	0.0000
$(\sin \theta/\lambda)_{\text{max}}$ (Å ⁻¹)	0.625

Refinement

$R[F^2 > 2\sigma(F^2)], wR(F^2), S$	0.075, 0.204, 1.05
No. of reflections	10766
No. of parameters	556
No. of restraints	214
H-atom treatment	H atoms treated by a mixture of independent and constrained refinement $w = 1/[\sigma^2(F_o^2) + (0.1028P)^2 + 37.7972P]$ where $P = (F_o^2 + 2F_c^2)/3$
$\Delta_{\text{max}}, \Delta_{\text{min}}$ (e Å ⁻³)	2.73, -2.43

D.5. Structural Data for $\text{Rh}_2(\text{tfepma})_2(p\text{-MeO-C}_6\text{H}_4\text{NC})(\mu\text{-Cl})\text{Cl}_3$ (**9**)

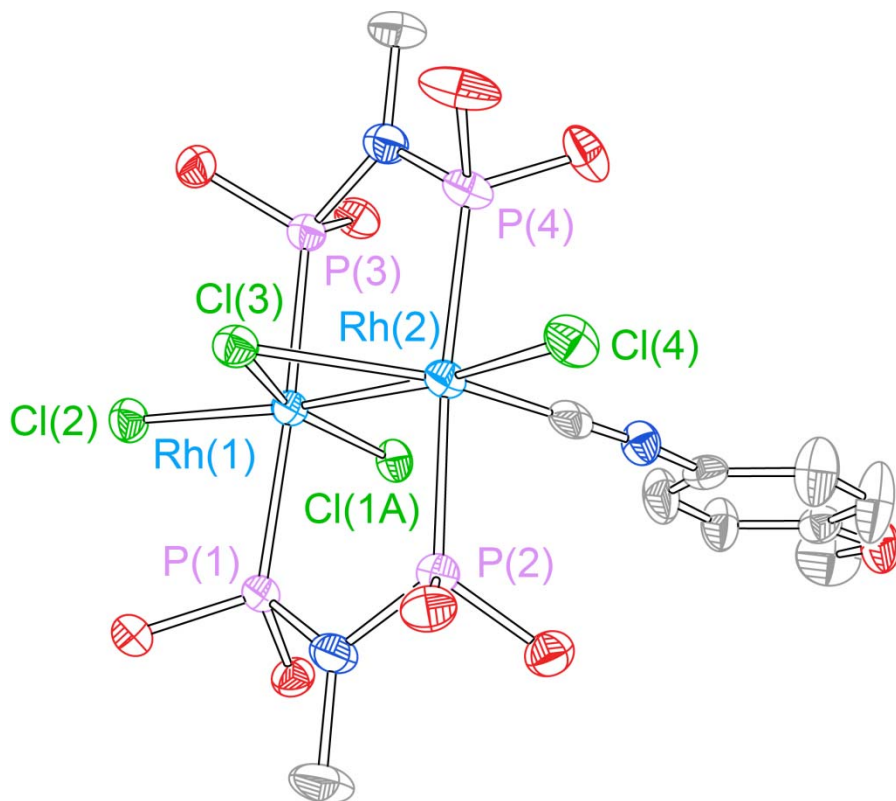


Figure S13. Thermal ellipsoid plot of **9** drawn at the 50% probability level. The $-\text{CH}_2\text{CF}_3$ groups and hydrogen atoms are omitted for clarity.

Table S5. X-ray experimental details for Rh₂(tfepma)₂(*p*-MeO-C₆H₄NC)(μ-Cl)Cl₃ (**9**)

Crystal data

Chemical formula	C ₃₃ H ₃₇ Cl ₄ F ₂₄ N ₃ O ₉ P ₄ Rh ₂
Fw, g/mol	1547.16
Crystal system, space group	Triclinic, <i>P</i> -1
Temperature (K)	100
<i>a</i> , <i>b</i> , <i>c</i> (Å)	10.7825 (5), 15.2029 (8), 18.7253 (9)
<i>a</i> , <i>b</i> , <i>g</i> (°)	87.983 (1), 80.065 (1), 73.223 (1)
<i>V</i> (Å ³)	2894.5 (2)
<i>Z</i>	2
Radiation type	Mo <i>K</i> α
μ (mm ⁻¹)	0.99
Crystal size (mm)	0.20 × 0.20 × 0.10

Data collection

Absorption correction	Multi-scan
<i>T</i> _{min} , <i>T</i> _{max}	0.827, 0.908
No. of measured, independent and observed [<i>I</i> > 2σ(<i>I</i>)] reflections	74141, 14427, 12029
<i>R</i> _{int}	0.038
(sin θ/λ) _{max} (Å ⁻¹)	0.667

Refinement

<i>R</i> [<i>F</i> ² > 2σ(<i>F</i> ²)], <i>wR</i> (<i>F</i> ²), <i>S</i>	0.054, 0.160, 1.05
No. of reflections	14427
No. of parameters	771
No. of restraints	502
H-atom treatment	H atoms treated by a mixture of independent and constrained refinement
	$w = 1/[\sigma^2(F_o^2) + (0.0783P)^2 + 11.7463P]$ where $P = (F_o^2 + 2F_c^2)/3$
Δ _{max} , Δ _{min} (e Å ⁻³)	2.76, -1.56

E. Steady-State Photolysis Data

E.1. Photolysis of 1 and 2

Stock solutions of Rh₂[I,III] complex **1** (17.6 mg, 1.07 × 10⁻⁵ mol) in 10.0 mL THF and Rh₂[II,II] complex **2** (6.4 mg, 3.3 × 10⁻⁶ mol) were prepared in an N₂-filled dry box. Reaction solutions were prepared by dilution of an appropriate volume of the stock solution with THF to 4.0 mL total volume. Reaction solutions were transferred to 1 cm quartz cuvettes and photolyzed with a 1000 W Hg/Xe arc lamp equipped with an appropriate long-pass filter. Reaction samples were periodically removed from the light source and UV-vis spectra were obtained. Photolysis continued until further evolution of Rh₂[0,II] complex **3** was no longer detected. Data obtained from these experiments is summarized in Figures S15, S16, and S17.

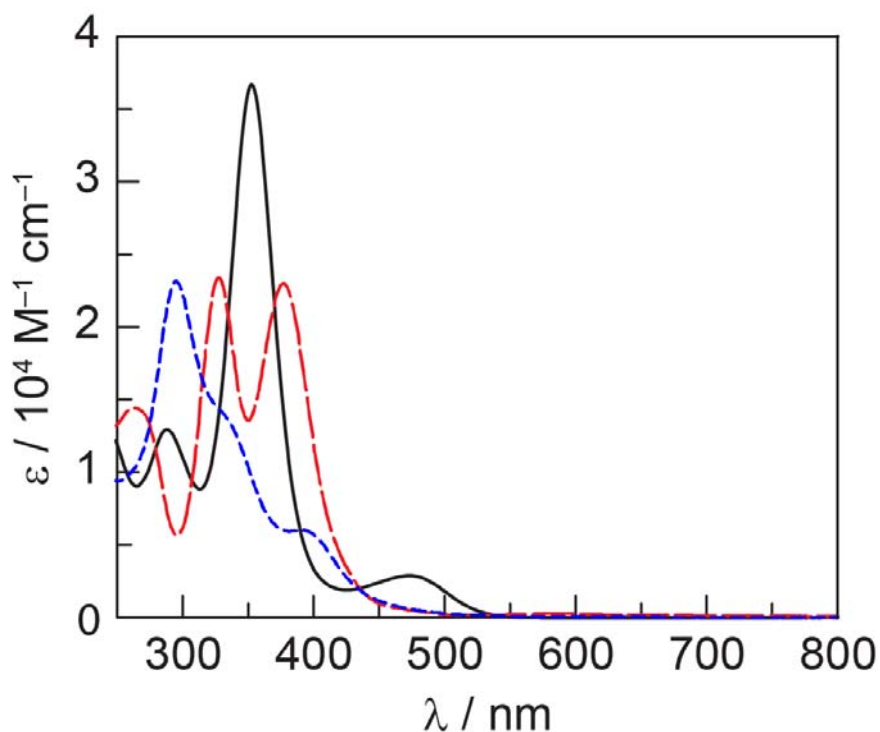


Figure S14. Extinction spectra of Rh₂[I,III] complex **1** (— —, red), Rh₂[II,II] complex **2** (black, —) and Rh₂[0,II] complex **3** (blue, — —) in THF.

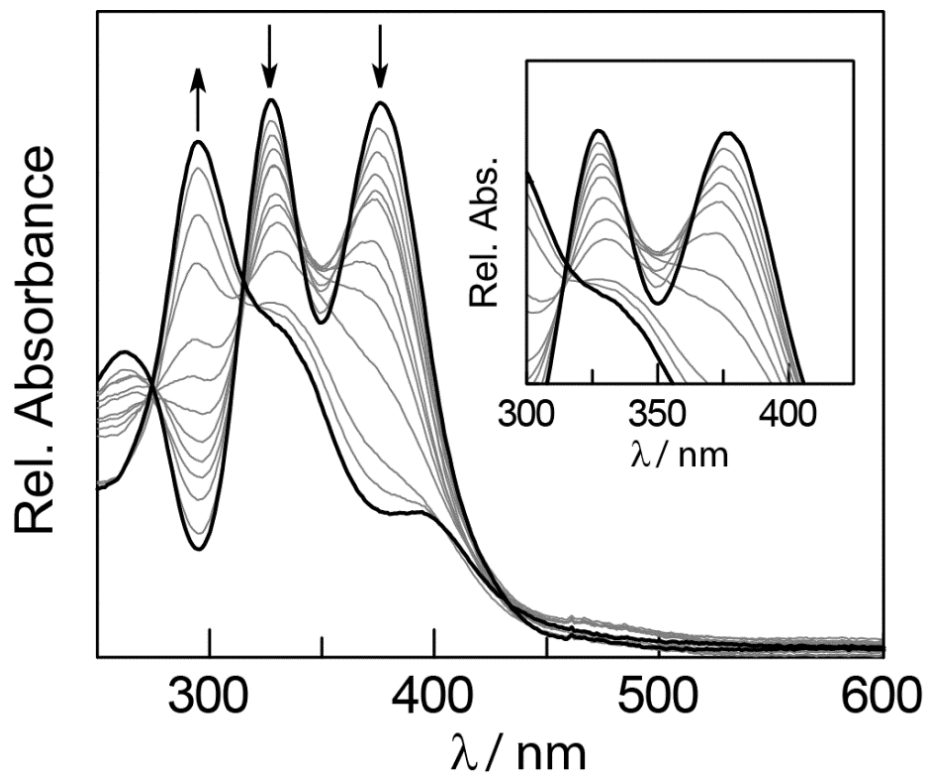


Figure S15. Spectral evolution for the photolysis of Rh₂[I,III] complex **1** in THF ($\lambda > 295$ nm). Spectra were collected periodically over 150 min. Inset: Isosbestic points were not observed in the spectra generated during the photolysis of **1**, consistent with the buildup of valence-isomer Rh₂[II,II] complex **2**.

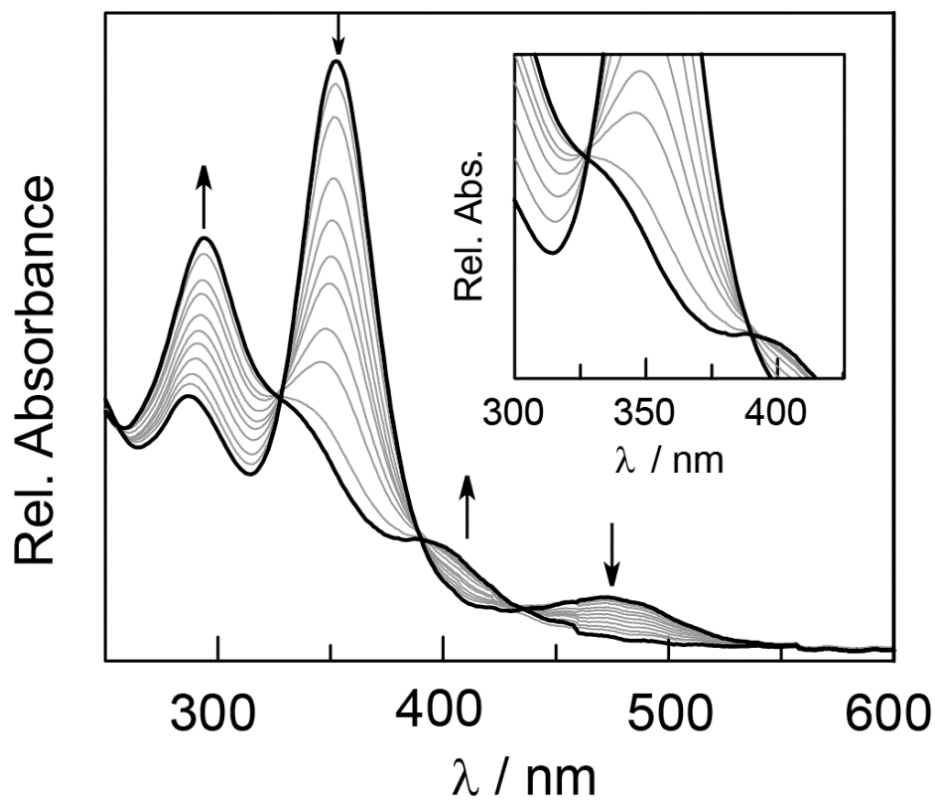


Figure S16. Spectral evolution for the photolysis of $\text{Rh}_2[\text{II},\text{II}]$ complex **2** in THF ($\lambda > 295$ nm). Spectra were collected periodically over 55 min. Inset: Isosbestic points were observed in the spectra generated during the photolysis of **1**, consistent with photoreduction of **2** without build-up of a steady-state intermediate.

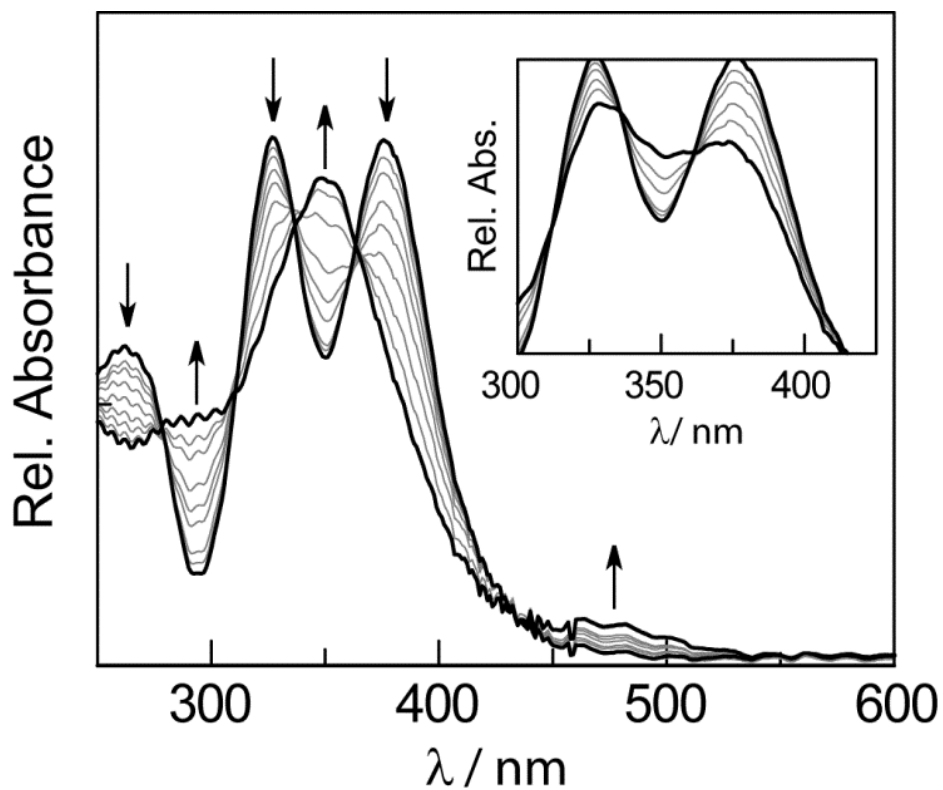


Figure S17. Spectral evolution for the first 600 min of photolysis of $\text{Rh}_2[\text{I,III}]$ complex **1** in THF ($\lambda > 380 \text{ nm}$). Inset: At early times in the photolysis of **1** with a 380 nm long-pass filter, isosbestic points are observed.

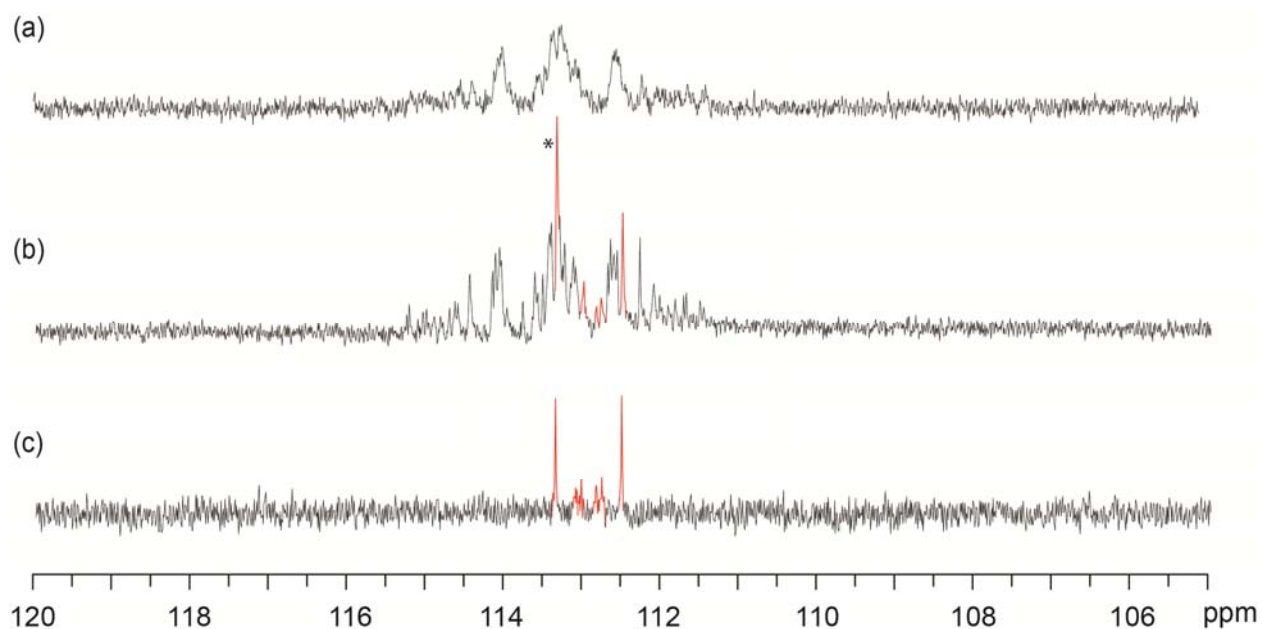


Figure S18. (a) ^{31}P NMR spectrum of $\text{Rh}_2[\text{I,III}]$ complex **1** recorded in THF at 23 °C. (b) ^{31}P NMR spectrum of a photolysis reaction recorded in THF at 23 °C; $\text{Rh}_2[\text{I,III}]$ complex **1** was photolyzed in an NMR tube and monitored periodically. The spectrum presented contains both $\text{Rh}_2[\text{I,III}]$ complex **1** and $\text{Rh}_2[\text{II,II}]$ complex **2** (resonances in red). (c) ^{31}P NMR spectrum of $\text{Rh}_2[\text{II,II}]$ complex **2** recorded in THF at 23 °C.

E.2. Spectral Fitting to Obtain Concentration Plots

In order to determine the concentration of reaction components during the photolysis reactions of complexes **1** and **2**, a least-squares spectral fitting algorithm was carried out. In order to accomplish this analysis, first, the wavelength-dependent molar absorptivity values of complexes **1**, **2**, and **3** were determined. The values are shown in S14. These molar absorptivity values, in combination with the UV-vis spectra that were obtained during photolysis (Figures S15 and S16) allowed the concentration of each reaction component to be determined at each time point for which a UV-vis spectrum was obtained. A model was used in which an absorbance was calculated for each wavelength using the equation:

$$A_{\lambda,\text{model}} = c_1\varepsilon_{1,\lambda} + c_2\varepsilon_{2,\lambda} + c_3\varepsilon_{3,\lambda} \quad (\text{S1})$$

A spreadsheet was then generated in which the difference between the computed A_λ and the experimentally observed A_λ was computed for a given set of concentrations (c_1 , c_2 , and c_3). This difference is the error between the computed model and the experimentally observed absorbance. By optimizing the concentrations of each of the reaction components, the square of the error was minimized:

$$(\text{Error})^2 = \sum_{300 \text{ nm}}^{450 \text{ nm}} (A_{\lambda,\text{model}} - A_{\lambda,\text{exp}})^2 \quad (\text{S2})$$

This protocol was repeated for each of the UV-vis spectra that were obtained during the photolysis of complex **1** and **2**. The concentrations of each reaction component in these photolysis reactions are plotted in Figures S19 and S20.

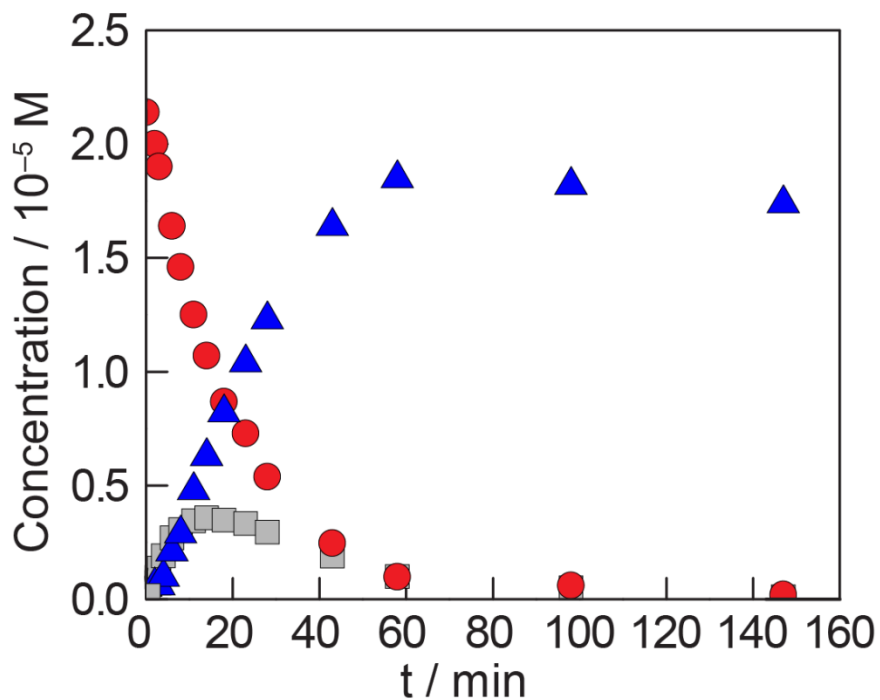


Figure S19. Concentration vs. time plot for the photolysis of Rh₂[I,III] complex **1** in THF ($\lambda > 295$ nm). The concentrations of each of the reaction components were determined by least-squares fitting of the experimental UV-vis spectra at each time point for **1** (red, ●), **2** (gray, ■) and **3** (blue, ▲).

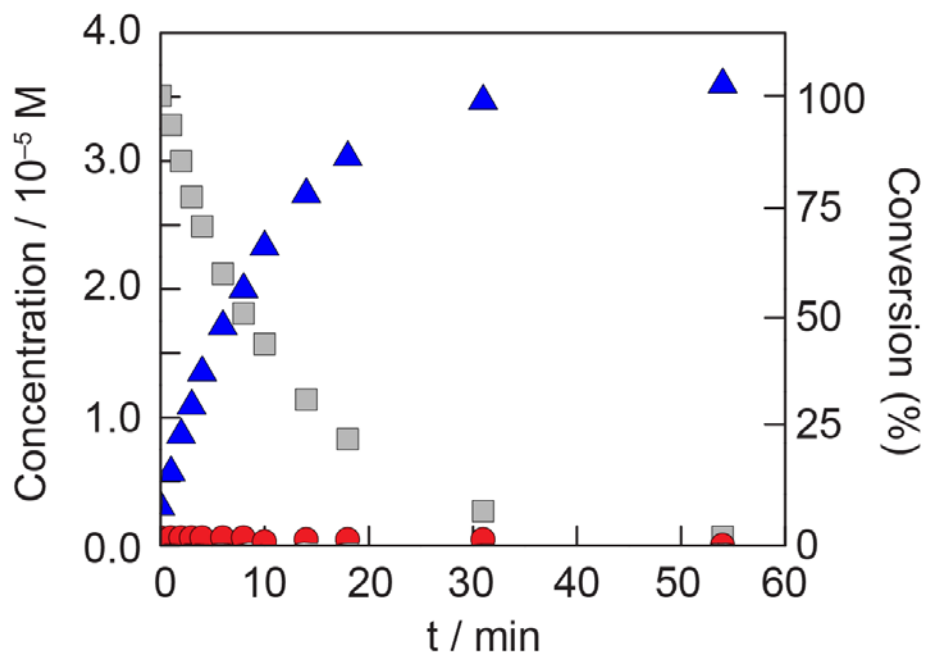


Figure S20. Concentration vs. time plot for the photolysis of Rh₂[II,II] complex **2** in THF ($\lambda > 295$ nm). The concentrations of each of the reaction components were determined by least-squares fitting of the experimental UV-vis spectra at each time point for **1** (red, ●), **2** (gray, ■) and **3** (blue, ▲).

E.3. Determination of Quantum Yields

Quantum yields were determined using 320 nm monochromatic light, which was generated with a 320 nm Hg line filter on a 1000 W Hg/Xe arc lamp. Potassium ferrioxalate was used as a chemical actinometer.⁵ The photo flux was determined from the average of actinometric measurements before and after irradiation of the reaction samples. Each quantum yield determination was carried out in triplicate. Experimental details are reported below.

The quantum yield for the photoconversion of **2** to **3** was determined by analyzing consumption of **2** as a function of photon flux. The following equation was used to determine the quantum yield:

$$\Phi = \frac{n_x t_{\text{Fe}} \Phi_{\text{Fe}} (1 - 10^{-A})_{\text{Fe}}}{n_{\text{Fe}} t_x \Phi_{\text{Fe}} (1 - 10^{-A})_x} \quad (\text{S3})$$

where n_x and n_{Fe} are the number of moles of **3** and Fe^{2+} generated during the photolysis reactions of **2** and ferrioxalate, respectively, t_x and t_{Fe} are the amounts of time that the samples of **3** and ferrioxalate were photolyzed for, Φ_{Fe} is the quantum yield of ferrioxalate reduction at 320 nm, and $(1-10^{-A})_x$ and $(1-10^{-A})_{\text{Fe}}$ are the fraction of incident light absorbed by the ferrioxalate standard and the reaction mixture during photolysis. The term $(1-10^{-A})_{\text{Fe}}$ was assumed to be unity and the term $(1-10^{-A})_x$ was calculated with the equation:

$$(1 - 10^{-A})_x = \frac{A_x}{A_{\text{tot}}} (1 - 10^{-A})_{\text{tot}} \quad (\text{S4})$$

where A_{tot} is the total absorbance of the sample at the exciting wavelength and A_x is the absorbance attributable to the starting material (**2** in this case), which was calculated using the known concentration of **2** and the molar absorptivity at the exciting wavelength.

The quantum yield of isomerization of **1** to **2** was determined during the reaction regime where the concentration of **2** was nearly constant; samples were photolyzed to ~20% consumption of **1** before quantum yield determinations were carried out. Using the equation:

$$\frac{d[\mathbf{2}]}{dt} = 0 = \Phi_{1,2}(1 - 10^{-A})_1 + \Phi_{2,3}(1 - 10^{-A})_2 \quad (\text{S5})$$

as well as the known concentrations of **A** and **B**, and the quantum yield of photoreduction of **2**, the quantum yield of isomerization was determined.

Finally, analysis of the early time points of the photolysis of **1** allowed an overall quantum

⁵ Montalti, M.; Credi, A.; Prodi, L.; Gandolfi, M. T. *Handbook of Photochemistry*, 3rd ed.; Taylor and Francis: Boca Raton, FL, 2006.

yield for consumption of **1** to be determined, using equation S6. This observed quantum yield, coupled with the equation:

$$\Phi_{\text{obs}} = \Phi_{1,2} + \Phi_{1,3}(1 - 10^{-A})_1 \quad (\text{S6})$$

allowed determination of the quantum yield of elimination from **1**.

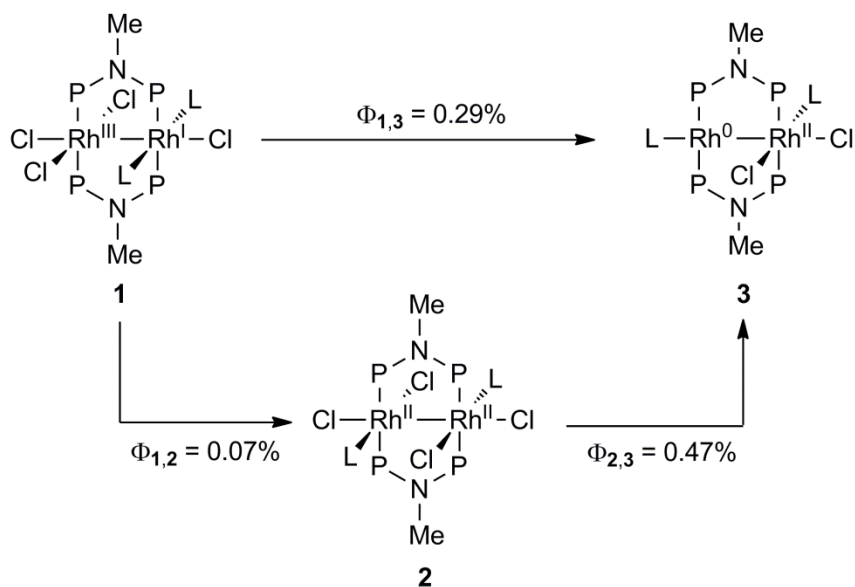


Figure S21. Experimentally determined quantum yields for photoreduction and photoisomerization reactions irradiated with 320 nm monochromatic light in THF.

The quantum yields for photoreduction of **8** ($\Phi_{320} = 0.80$) and **9** ($\Phi_{320} = 0.58$) were determined by similar procedures used to determine the quantum yield of complex **2**.

E.4. Steady-State Photolysis of $\text{Rh}_2(\text{tfepma})_2(p\text{-F-C}_6\text{H}_4\text{NC})(\mu\text{-Cl})\text{Cl}_3$ (**8**)

Extinction spectra of complexes **6** and **8** are shown in Figure S22. A stock solution of $\text{Rh}_2(\text{tfepma})_2(p\text{-F-C}_6\text{H}_4\text{NC})(\mu\text{-Cl})\text{Cl}_3$ (**8**) (15.1 mg, 1.05×10^{-5} mol) in 15.0 mL THF was prepared in an N_2 -filled dry box. Reaction solutions were prepared by dilution of an appropriate volume of the stock solution with THF to 4.0 mL total volume. Reaction solutions were transferred to 1 cm quartz cuvettes and photolyzed with a 1000 W Hg/Xe arc lamp equipped with a 305 nm long-pass filter. Reaction samples were periodically removed from the light source and UV-vis spectra were obtained to give Figure S23. Photolysis continued until further evolution of $\text{Rh}_2[\text{I},\text{I}]$ complex **6** was no longer detected.

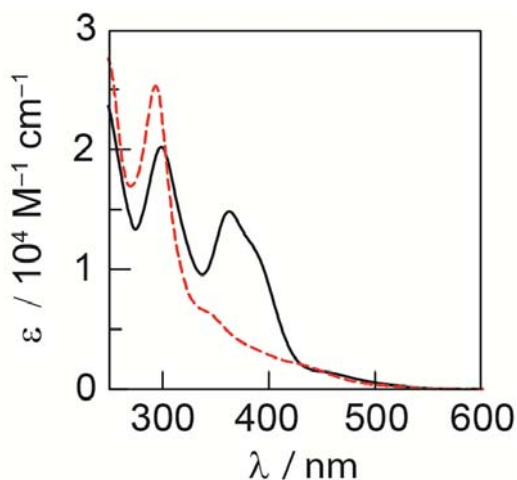


Figure S22. Extinction spectra of **8** (black, —) and **6** (red, ---) in THF.

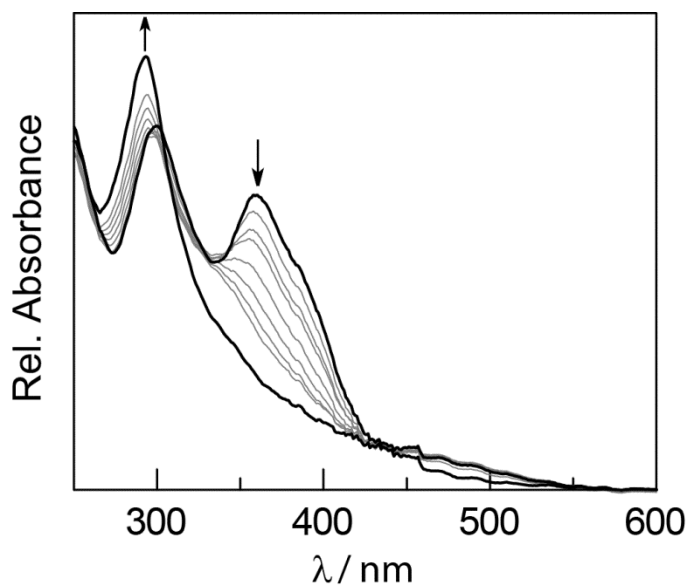


Figure S23. Spectral evolution for the photolysis of $\text{Rh}_2(\text{tfepma})_2(p\text{-F-C}_6\text{H}_4\text{NC})(\mu\text{-Cl})\text{Cl}_3$ (**8**) in THF ($\lambda > 295$ nm). Spectra were collected periodically over 100 min.

E.5. Thermolysis of $\text{Rh}_2(\text{tfepma})_2(p\text{-F-C}_6\text{H}_4\text{NC})(\mu\text{-Cl})\text{Cl}_3$ (**8**)

A stock solution of $\text{Rh}_2(\text{tfepma})_2(p\text{-F-C}_6\text{H}_4\text{NC})(\mu\text{-Cl})\text{Cl}_3$ (**8**) (15.1 mg, 1.05×10^{-5} mol) in 15.0 mL THF was prepared in an N_2 -filled dry box. The reaction solution was prepared by dilution of 0.25 mL of the stock solution with 4.0 mL THF. The reaction solution was transferred to a 1 cm quartz cuvette. An absorption spectrum was obtained. The reaction vessel was wrapped in aluminum foil and heated to 80 °C for 3 h. An absorption spectrum of the reaction solution was obtained. Comparison of the absorption spectra obtained before and after heating indicated that no reaction had occurred.

F. Time-Resolved Photochemical Experiments

F.1. General Considerations

THF solutions of complexes **1** and **2** were prepared in 50-mL Schlenk flasks in an N_2 -filled glovebox. Solutions were flowed through a 3-mm diameter, 1-cm path length flow cell (Starna, type 585.2) using a peristaltic pump and positive argon pressure. Nanosecond transient absorption (TA) measurements were made with the pump light provided by the third harmonic (355 nm) of a Quanta-Ray Nd:YAG laser (Spectra-Physics) running at 10 Hz. Probe white light was provided by a 75 W Xe-arc lamp (Photon Technologies Inc.). The signal light passed through a Triax 320 spectrometer, where it was dispersed by a 300 nm \times 250 nm blazed grating and collected with either an intensified gated CCD camera (ICCD, CCD 30-11, Andor Technology, 1024 \times 256 pixels, 26 μm^2) for TA spectra or a photomultiplier tube (PMT) for TA single-wavelength kinetics. PMT outputs were collected and averaged with a 1GHz oscilloscope (LeCroy 9384CM). A TTL pulse synchronized with the Q-switch of the Infinity laser was delayed 99 ms before triggering the shutter for the probe light. Electronic delays were created with SRS DG535 delay generators (Stanford Research Systems). These delay boxes, in combination with electronic shutters (Uniblitz), were used to create the necessary pulse sequence.

Relevant spectral and kinetic data are compiled below.

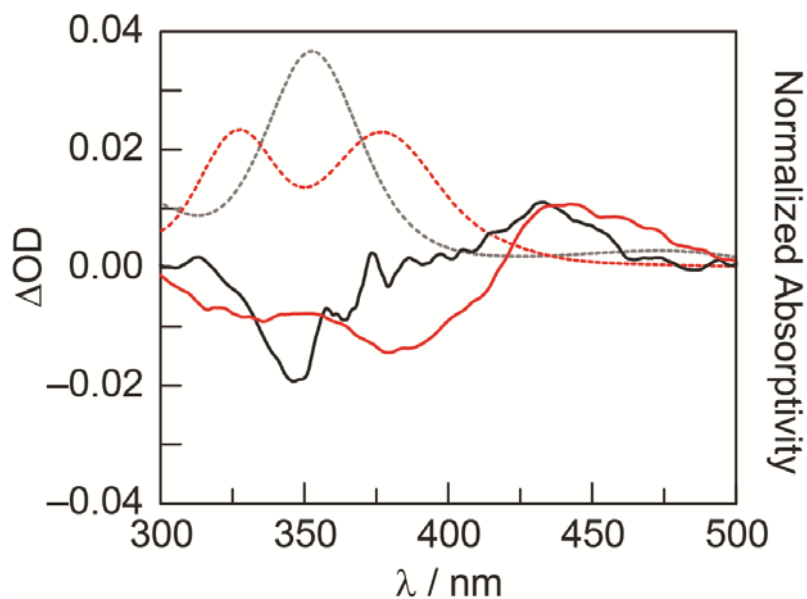


Figure S24. Transient absorption spectra obtained by laser flash photolysis (355 nm pump) of complexes **1** (solid red) and **2** (solid black), respectively, in THF. Spectra are normalized to the absorbance at ~ 440 nm. Normalized absorption spectra of **1** (dashed red) and **2** (dashed black) are also shown.

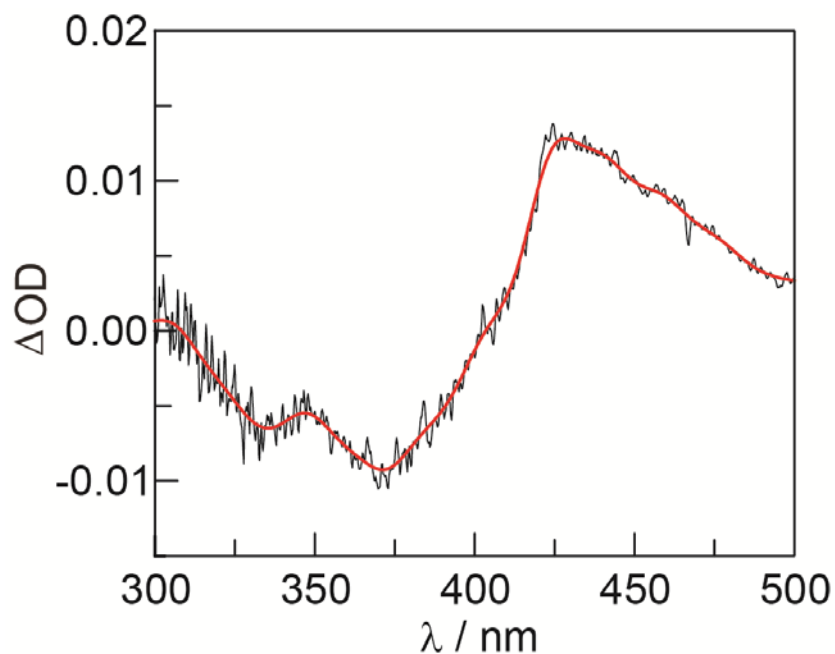


Figure S25. Transient absorption spectrum obtained by flash laser photolysis (355 nm pump) of complex **1** in THF. Raw data are shown in black and a Fourier fit of the data is shown in red.

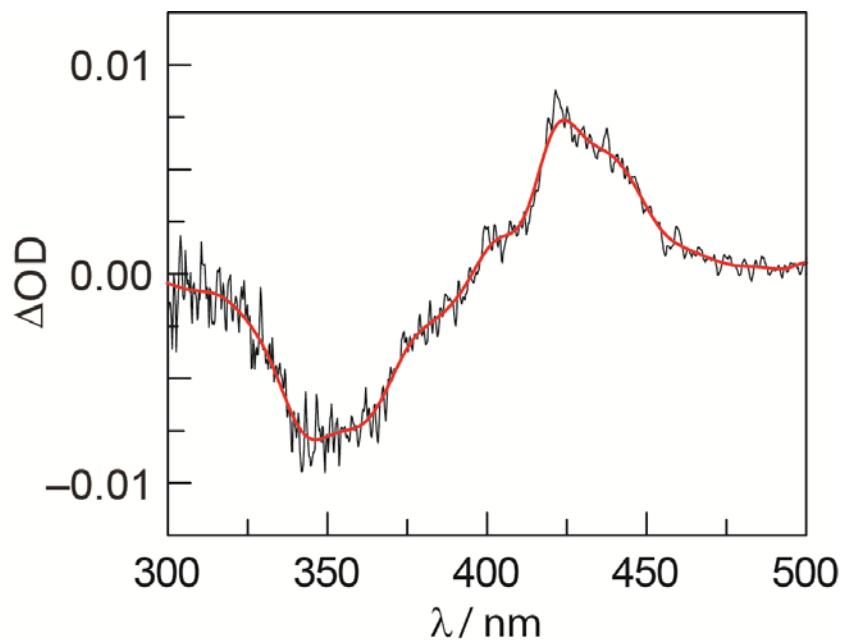


Figure S26. Transient absorption spectrum obtained by flash laser photolysis (355 nm pump) of complex **2** in THF. Raw data are shown in black and a Fourier fit of the data is shown in red.

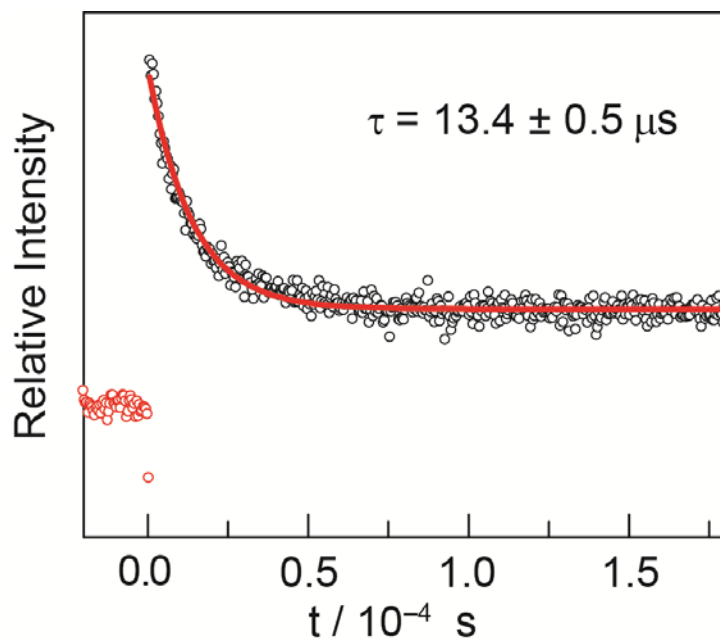


Figure S27. Single wavelength kinetic trace of a THF solution of complex **1** pumped at 355 nm and recorded at 437 nm.

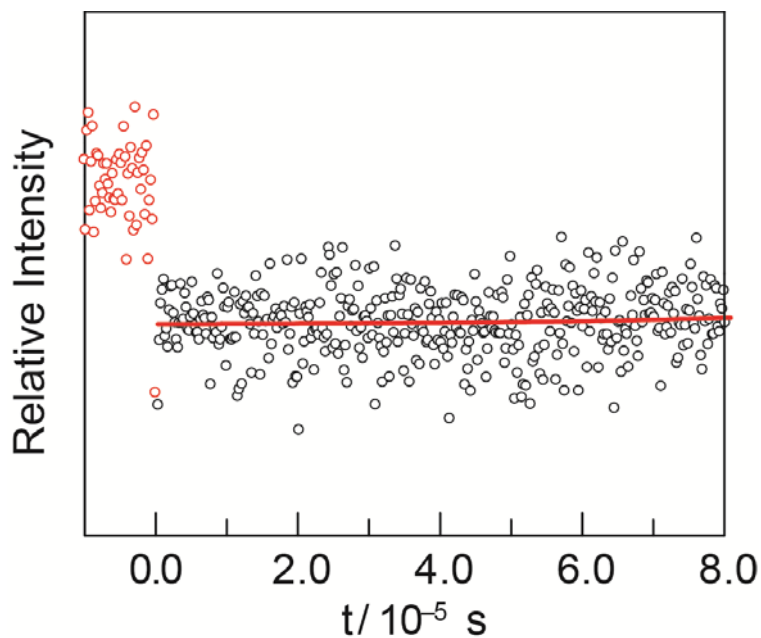


Figure S28. Single wavelength kinetic trace of a THF solution of complex **1** pumped at 355 nm and recorded at 380 nm.

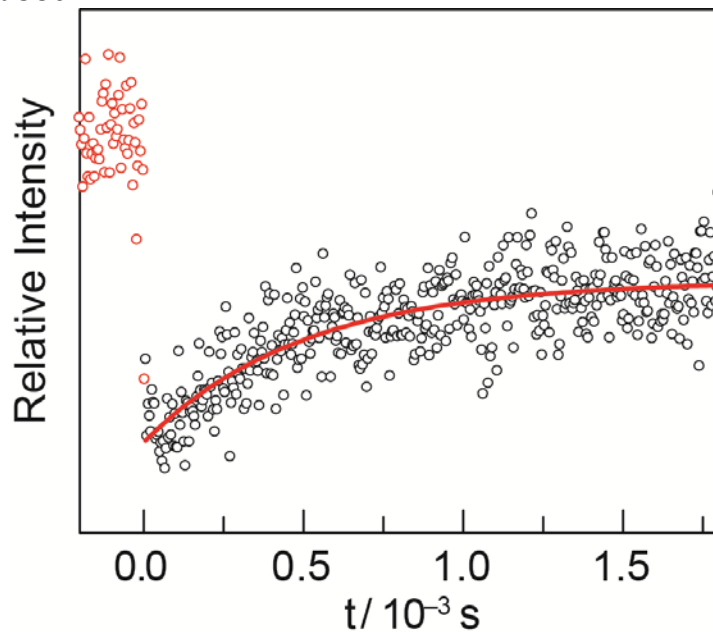


Figure S29. Single wavelength kinetic trace of a THF solution of complex **1** pumped at 355 nm and recorded at 380 nm.

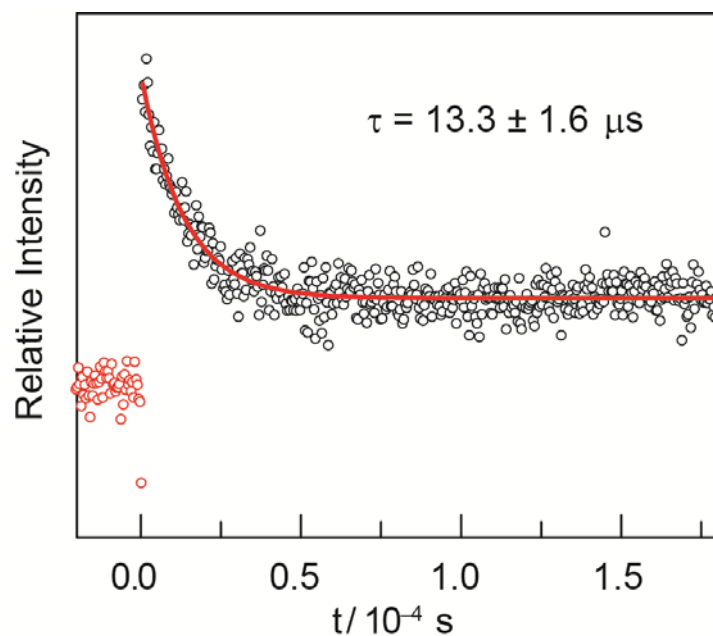


Figure S30. Single wavelength kinetic trace of a THF solution of complex **2** pumped at 355 nm and recorded at 437 nm.

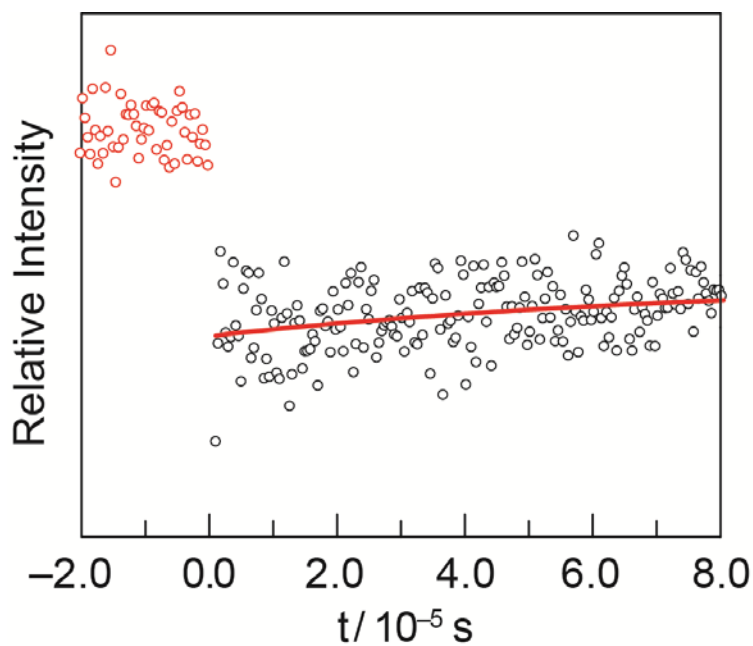


Figure S31. Single wavelength kinetic trace of a THF solution of complex **2** pumped at 355 nm and recorded at 330 nm.

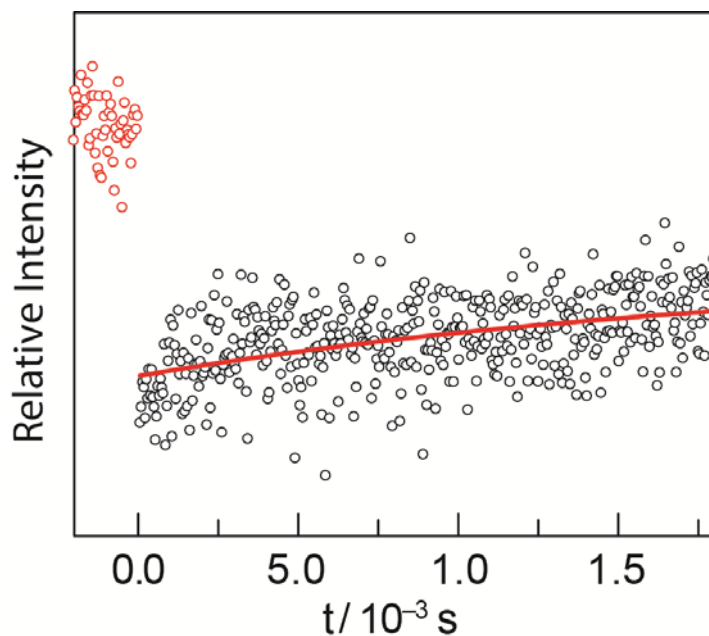


Figure S32. Single wavelength kinetic trace of a THF solution of complex **2** pumped at 355 nm and recorded at 330 nm.

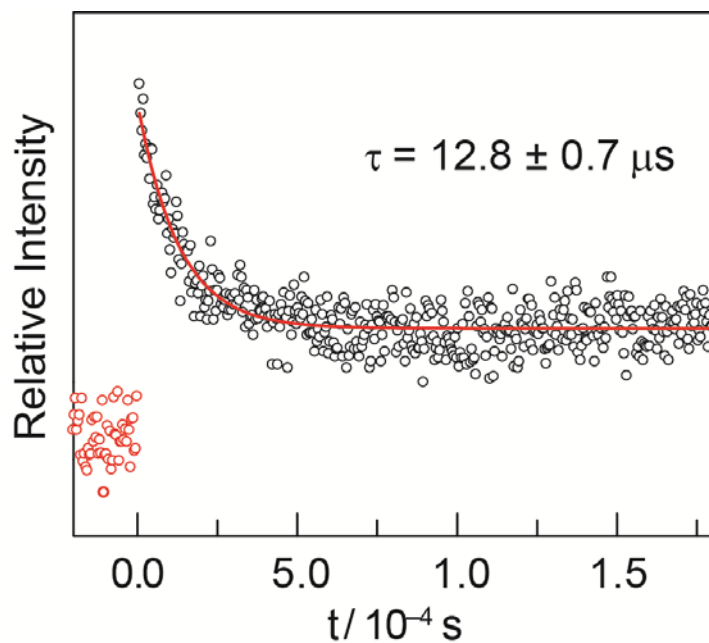


Figure S33. Single wavelength kinetic trace of a THF solution of complex **1** pumped at 355 nm and recorded at 437 nm. This spectrum was recorded in the presence of 1000 molar equivalents of adamantyl isocyanide.

F.2. Comparison of Absorption Spectra of Transient Intermediate with Chloride-Bridged Structures

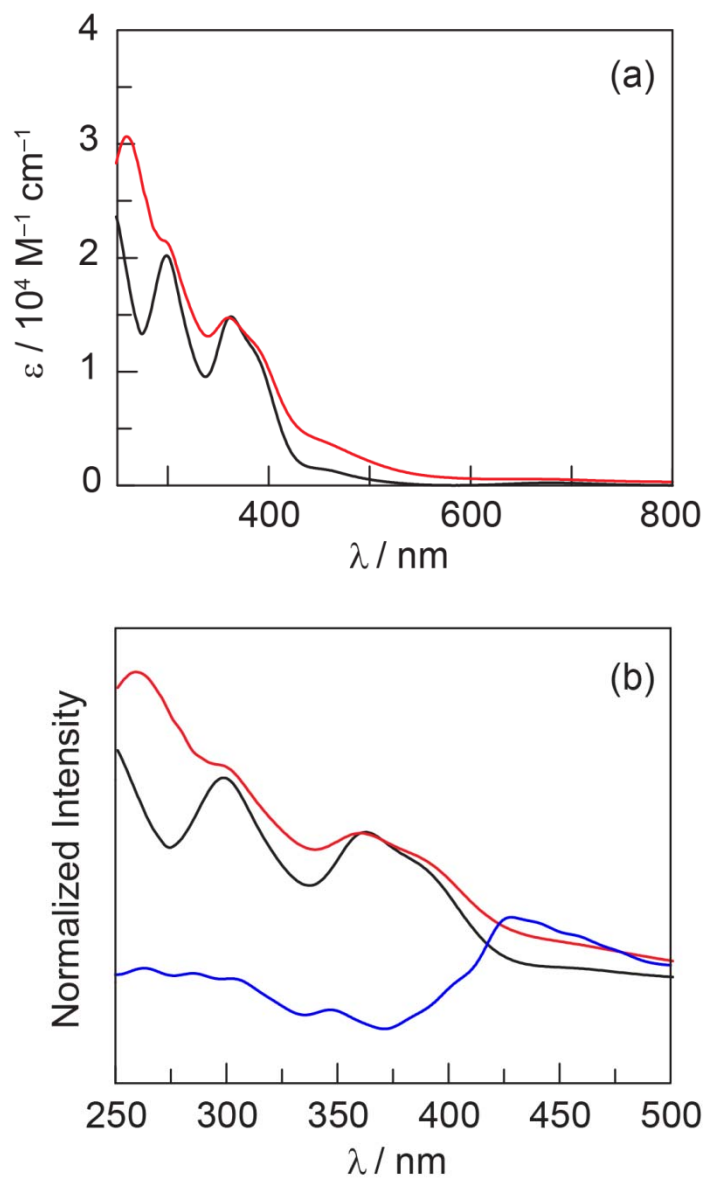


Figure S34. (a) Extinction spectra of chloride-bridged dirhodium complexes **8** (black) and **9** (red) in THF. (b) Extinction spectra of complexes **8** (black) and **9** (red) overlaid with the transient absorption spectrum obtained by pumping a THF solution of **1** at 355 nm (blue).

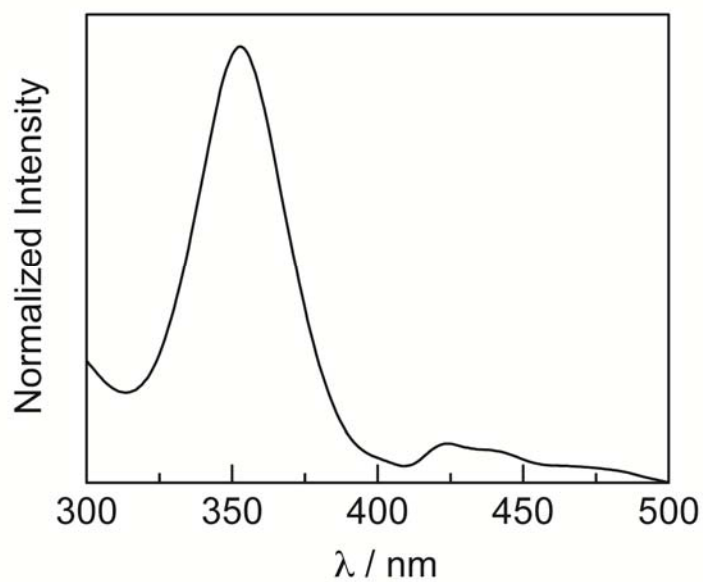


Figure S35. Spectrum of photointermediate **5** generated by addition of the absorption spectrum of **2** to the TA spectrum obtained upon laser flash photolysis of **2**. The spectrum shows a low intensity feature at ~440 nm.

G. Computational Analysis

G.1. Computational Methods

Density functional theory (DFT) calculations were performed with the hybrid functional Becke-3 parameter exchange functional⁶ and the Lee-Yang-Parr non-local correlation functional (B3LYP)⁷ as implemented in the Gaussian 03, Revision B.05 software package.⁸ An effective core potential (ECP) representing the 1s2s2p core was used for rhodium (LANL2DZ).⁹ The 6-31G* basis set¹⁰ was used for hydrogen, carbon, phosphorus, fluorine and chloride. All geometry optimizations were performed in C1 symmetry with subsequent vibrational frequency analysis to confirm that each stationary point was a minimum on the potential energy surface. The calculations were performed on simplified models of **1**, **2**, and **5** in which the CF₃CH₂O⁻ functional groups of tfepma have been replaced by F⁻ (dfpma) and the adamantyl functional groups of adamantly isocyanide have been replaced by CH₃. Orbitals were visualized using *Molekel* 5.3.¹¹

The percentage of rhodium, chloride, dfpma, and MeNC character in the occupied (canonical) molecular orbitals (MO's) and virtual orbitals discussed for complexes **A**, **B**, and **C** from a full population analysis using Eq. S7:

$$\% \text{Orbital Character}(i) = \frac{\sum \varphi_{(i)}^2}{\sum \varphi_{(all)}^2} \times 100 \quad (\text{S7})$$

Where $\sum \varphi_{(i)}^2$ ($i = \text{Rh, Cl, P, F, C, H}$) is the sum of the squares of the eigenvalues associated with the atomic orbitals (AO's) of interest and $\sum \varphi_{(all)}^2$ is the sum of the squares of the eigenvalues of all AO's in a particular MO.

⁶ (a) Becke, A. D. *Phys. Rev. A* **1988**, *38*, 3098. (b) Becke, A. D. *J. Chem Phys.* **1993**, *98*, 1372. (c) Becke, A. D. *J. Chem. Phys.* **1993**, *98*, 5648.

⁷ Lee, C.; Yang, W.; Parr, R. G. *Phys. Rev. B* **1988**, *37*, 785.

⁸ Gaussian 03, Revision B.05, Frisch, M. J.; Trucks, G. W.; Schlegel, H. B.; Scuseria, G. E.; Robb, M. A.; Cheeseman, J. R.; Montgomery, Jr., J. A.; Vreven, T.; Kudin, K. N.; Burant, J. C.; Millam, J. M.; Iyengar, S. S.; Tomasi, J.; Barone, V.; Mennucci, B.; Cossi, M.; Scalmani, G.; Rega, N.; Petersson, G. A.; Nakatsuji, H.; Hada, M.; Ehara, M.; Toyota, K.; Fukuda, R.; Hasegawa, J.; Ishida, M.; Nakajima, T.; Honda, Y.; Kitao, O.; Nakai, H.; Klene, M.; Li, X.; Knox, J. E.; Hratchian, H. P.; Cross, J. B.; Bakken, V.; Adamo, C.; Jaramillo, J.; Gomperts, R.; Stratmann, R. E.; Yazyev, O.; Austin, A. J.; Cammi, R.; Pomelli, C.; Ochterski, J. W.; Ayala, P. Y.; Morokuma, K.; Voth, G. A.; Salvador, P.; Dannenberg, J. J.; Zakrzewski, V. G.; Dapprich, S.; Daniels, A. D.; Strain, M. C.; Farkas, O.; Malick, D. K.; Rabuck, A. D.; Raghavachari, K.; Foresman, J. B.; Ortiz, J. V.; Cui, Q.; Baboul, A. G.; Clifford, S.; Cioslowski, J.; Stefanov, B. B.; Liu, G.; Liashenko, A.; Piskorz, P.; Komaromi, I.; Martin, R. L.; Fox, D. J.; Keith, T.; Al-Laham, M. A.; Peng, C. Y.; Nanayakkara, A.; Challacombe, M.; Gill, P. M. W.; Johnson, B.; Chen, W.; Wong, M. W.; Gonzalez, C.; and Pople, J. A.; Gaussian, Inc., Wallingford CT, 2004.

⁹ (a) Wadt, W. R.; Hay, P. J. *J. Chem. Phys.* **1985**, *82*, 284. (b) Hay, P. J.; Wadt, W. R. *J. Chem. Phys.* **1985**, *82*, 299.

¹⁰ Hehre, W. J.; Random, L.; Schleyer, P. v. R.; Pople, J. A. *Ab Initio Molecular Orbital Theory*; John Wiley: New York, 1986.

¹¹ Flükiger, P.; Lüthi, H.P.; Portmann, S.; Weber, J. *MOLEKEL*, 5.3; Swiss Center for Scientific Computing; Manno, Switzerland, 2000; www.cscs.ch/molekel.

The vertical singlet transition energies of the complexes were computed at the time-dependent density functional theory (TD-DFT) level within G03 using the ground state optimized structures. Contribution of a specific electronic transition to an excitation of interest was calculated using Eq S8:

$$\% \text{Contribution of Transition}(i) = \frac{C_{(i)}^2}{\sum C_{(all)}^2} \times 100 \quad (\text{S8})$$

Where $C_{(i)}^2$ is the square of the configuration interaction coefficient calculated by G03 for a particular electronic transition and $\sum C_{(all)}^2$ is the sum of the squares of all of the configuration interaction coefficients for specific electronic transitions in a particular excitation.

G.2. Cartesian Coordinates of Computed Structures

Table S6. Cartesian coordinates for the geometry-optimized structure of Rh₂(I,III) structure **A**

Atom Type	x	y	z
Rh	-0.000234	-1.376129	0.000455
Rh	0.000186	1.423585	-0.000429
Cl	0.515702	1.438466	-2.373809
P	2.269383	1.444223	0.292403
Cl	-0.515296	1.440176	2.372967
Cl	-0.000594	-3.902444	0.001151
P	2.195054	-1.261829	-0.697643
Cl	0.000531	3.865951	-0.001215
P	-2.195495	-1.260762	0.698508
P	-2.268992	1.444632	-0.293353
N	3.109357	0.099980	-0.329792
N	-3.109377	0.101106	0.329850
C	0.624816	-1.418560	1.894690
N	-0.983400	-1.518804	-2.994239
N	0.983225	-1.516551	2.995171
C	-0.625263	-1.419673	-1.893778
C	-1.304353	-1.422426	-4.374652
H	-1.012408	-0.429620	-4.727578
H	-0.762666	-2.193372	-4.927437
H	-2.378368	-1.566941	-4.511453
C	1.304552	-1.417699	4.375334
H	1.012388	-0.424351	4.726553
H	0.763279	-2.187846	4.929632
H	2.378653	-1.561642	4.512062
F	-2.874935	1.553170	-1.760794
F	-3.110471	2.615592	0.352347
F	3.111163	2.614449	-0.354233
F	2.875433	1.553726	1.759733
F	3.147533	-2.392816	-0.112534
F	2.502817	-1.526995	-2.234081
F	-2.503317	-1.524902	2.235107
F	-3.148309	-2.391824	0.114086
C	-4.586160	0.099575	0.513152
H	-4.931394	1.131420	0.564110

H	-5.076051	-0.418518	-0.313562
H	-4.831066	-0.390349	1.457045
C	4.586140	0.097867	-0.513090
H	5.075855	-0.419959	0.313895
H	4.830889	-0.392628	-1.456728
H	4.931719	1.129569	-0.564585

Table S7. Cartesian coordinates for the geometry-optimized structure of Rh₂(II,II) structure **B**

Atom Type	x	y	z
Rh	-0.037038	1.352321	0.336989
Rh	0.006134	-1.345156	-0.333088
Cl	0.062558	-3.788132	-0.820623
Cl	-0.716281	-0.844724	-2.611629
Cl	-0.055959	3.796562	0.814340
Cl	-0.731238	0.838159	2.620233
P	-2.294687	1.403909	-0.092036
P	-2.247599	-1.466166	0.096135
P	2.194546	1.190617	0.856094
P	2.231627	-1.138846	-0.859235
N	-3.152840	-0.043827	0.021304
N	3.097274	0.081632	-0.058298
N	0.645317	2.211308	-2.575874
N	0.714314	-2.182238	2.579792
C	-4.639778	-0.088208	-0.022476
H	-5.026769	0.881357	0.289523
H	-4.996400	-0.841791	0.681410
H	-4.984424	-0.324031	-1.030905
C	4.585922	0.078916	-0.056916
H	4.940052	1.086480	0.159030
H	4.942370	-0.207885	-1.047497
H	4.970257	-0.619699	0.688916
C	0.460445	-1.823638	1.503126
C	0.401192	1.842803	-1.500232
F	-3.189212	2.344461	0.808413
F	-2.751852	1.993668	-1.497913
F	-2.685991	-2.095033	1.491106
F	-3.120068	-2.408826	-0.821976
F	2.651606	0.875894	2.344299
F	3.084525	2.486930	0.642971
F	2.691809	-0.938062	-2.364652
F	3.161616	-2.381530	-0.527647
C	0.795310	2.432886	-3.971031
H	0.192853	3.294577	-4.267904
H	1.844716	2.630630	-4.201145

H	0.458208	1.536773	-4.499287
C	0.871472	-2.389277	3.976472
H	0.512112	-1.497691	4.497671
H	0.291459	-3.263684	4.280716
H	1.925841	-2.558408	4.206559

Table S8. Cartesian coordinates for the geometry-optimized structure of chloride-bridged structure **C**

Atom Type	x	y	z
Rh	-0.001059	-1.294827	-0.273732
Rh	0.002915	1.36477	0.009499
Cl	0.007963	1.503903	2.394641
P	-2.286203	1.516855	-0.006945
Cl	-0.007057	0.262467	-2.237931
Cl	-0.018787	-3.623845	-1.175048
P	-2.305492	-1.36036	-0.307739
Cl	-0.008427	3.792458	-0.356847
P	2.304202	-1.364425	-0.31279
P	2.294471	1.511853	-0.019062
N	-3.169969	0.071896	-0.152565
N	3.17053	0.073573	-0.253253
N	0.003479	-2.162635	2.691281
C	0.000822	-1.834	1.576039
C	0.003896	-2.412974	4.090115
H	0.012806	-1.457805	4.620954
H	-0.891936	-2.97853	4.357407
H	0.889905	-2.995107	4.353948
F	3.053032	2.141113	1.217372
F	2.943493	2.417508	-1.142932
F	-3.030852	2.208809	1.203756
F	-2.943234	2.366578	-1.168897
F	-3.000005	-2.013186	-1.568231
F	-2.97989	-2.281058	0.800979
F	2.993034	-2.089873	-1.536938
F	2.979976	-2.226377	0.842859
C	4.657212	0.090204	-0.352312
H	4.96543	1.009644	-0.850628
H	5.10521	0.034749	0.641715
H	4.982515	-0.755999	-0.957653
C	-4.650818	0.096949	-0.314947
H	-4.919354	0.224836	-1.365044
H	-5.068169	-0.835745	0.066275
H	-5.052312	0.920466	0.27639

G.3. Comparison of Computed Structures and X-ray Structures

Table S9. Structural comparison between the empirical structure of **1** and the calculated structure of **A**. All cis bond angles in the primary coordination sphere are approximately 90°.

Measurement	1	A
d (Rh–Rh)	2.71 Å	2.80 Å
avg. d (Rh–Cl _{eq})	2.36 Å	2.43 Å
d (Rh ^I –Cl _{ap})	2.49 Å	2.53 Å
d (Rh ^{III} –Cl _{ap})	2.45 Å	2.44 Å
avg. d (Rh–CNR)	1.99 Å	2.00 Å
avg. d (Rh ^I –P)	2.29 Å	2.31 Å
avg. d (Rh ^{III} –P)	2.28 Å	2.29 Å
Torsion Angle (P–Rh–Rh–P)	28.15°	25.00°

Table S10. Structural comparison between the empirical structure of **2** and the calculated structure of **B**. All cis bond angles in the primary coordination sphere are approximately 90°.

Measurement	2	B
d (Rh–Rh)	2.72 Å	2.78 Å
avg. d (Rh–Cl _{eq})	2.38 Å	2.44 Å
avg. d (Rh–Cl _{ap})	2.47 Å	2.49 Å
avg. d (Rh–CNR)	1.95 Å	1.95 Å
avg. d (Rh–P)	2.28 Å	2.30 Å
Torsion Angle (P–Rh–Rh–P)	23.44°	24.86°

H. Time-Dependent DFT Analysis

H.1. Excited State Calculation of Rh₂[I,III] Structure A

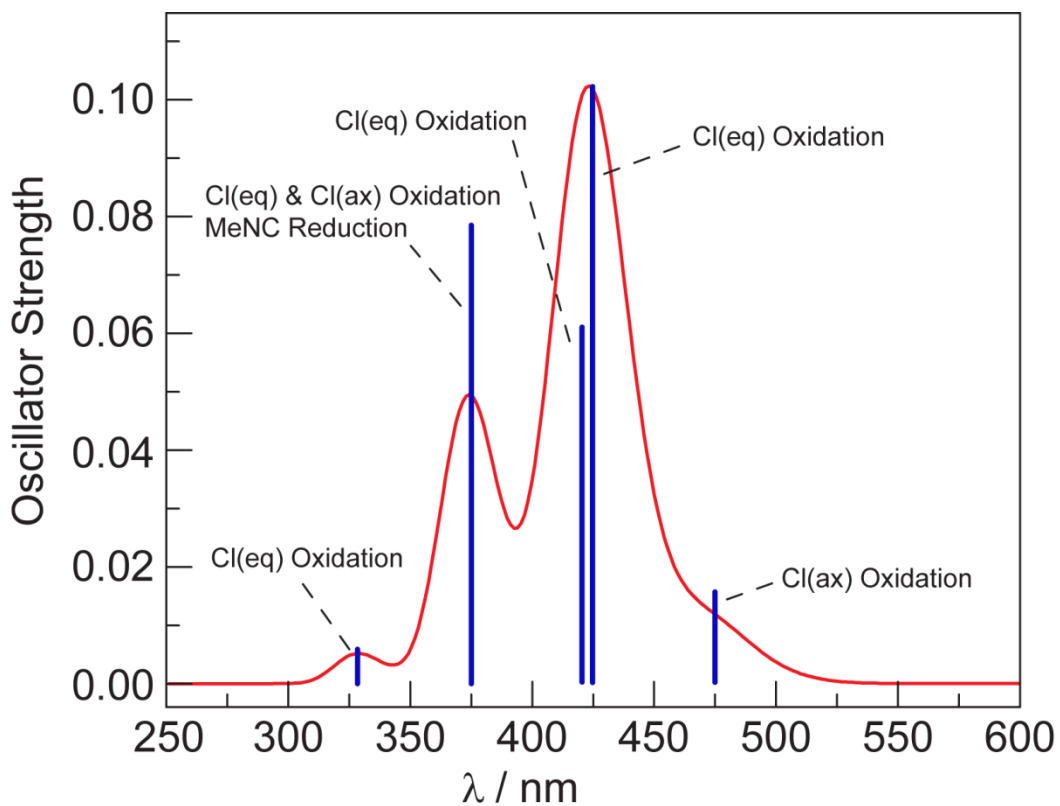


Figure S36. Relevant oscillators (solid blue bars) from TD-DFT calculations for **A** with simulated absorption spectrum overlaid (solid red line).

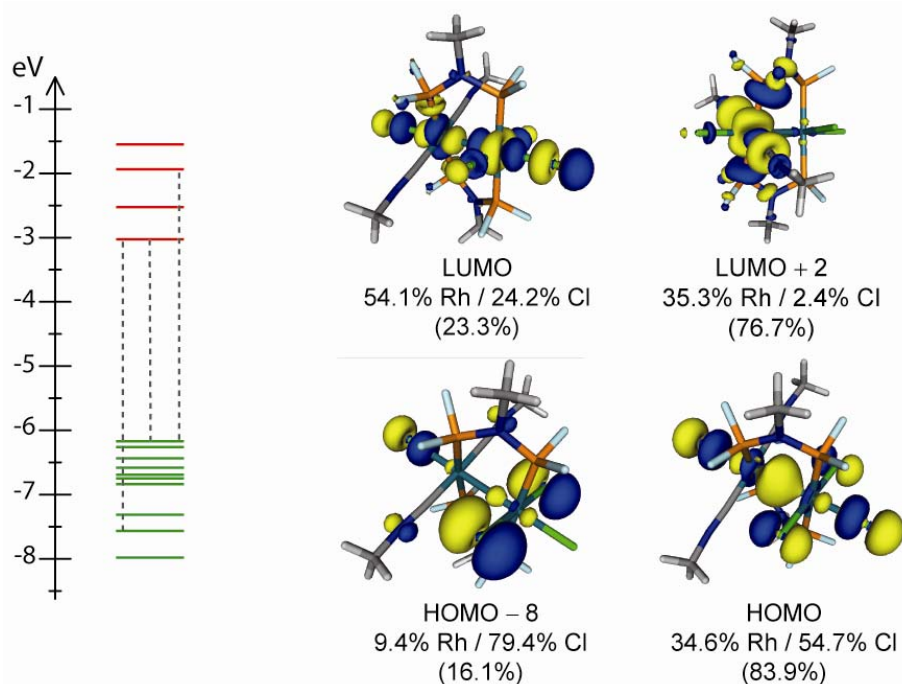


Figure S37. Excitation profile for 374 nm excitation of **A**. The molecular orbital manifold (left) is presented with filled orbitals shown in green and empty orbitals shown in red. Contributing electronic transitions to the overall excitation are noted with dashed lines. Contributing MO's to the excitation are presented (right). The percent contribution of Rh and Cl are shown directly underneath the MO label with the contribution of the MO to the total excitation presented within parenthesis.

Table S11. Origin of atomic orbitals that contribute to molecular orbital ground state and excited state for 374 nm excitation of **A**.

	Ground State Composite Orbital	Excited State Composite Orbital	Difference
Rh(I)	22.0%	31.4%	+9.4%
Rh(III)	8.6%	8.3%	-0.3%
Equatorial Cl's	26.5%	1.8%	-24.7%
Axial Cl's	32.2%	5.7%	-26.5%
dfpma	3.9%	35.8%	+31.9%
MeNC	5.3%	17.0%	+11.7%

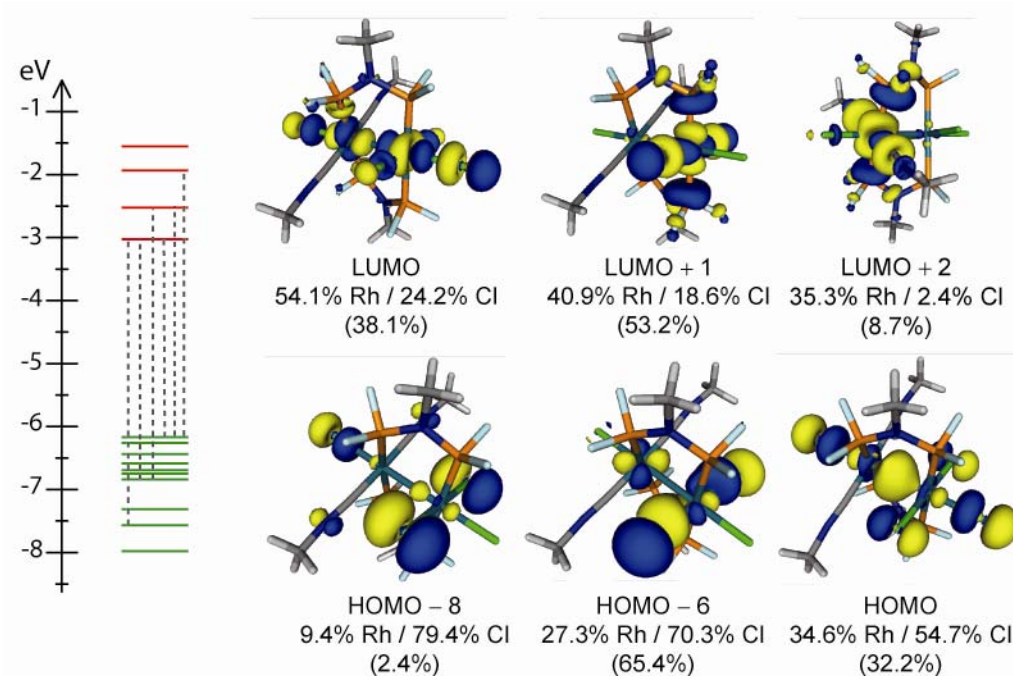


Figure S38. Excitation profile for 420 nm excitation of **A**. The molecular orbital manifold (left) is presented with filled orbitals shown in green and empty orbitals shown in red. Contributing electronic transitions to the overall excitation are noted with dashed lines. Contributing MO's to the excitation are presented (right). The percent contribution of Rh and Cl are shown directly underneath the MO label with the contribution of the MO to the total excitation presented within parenthesis.

Table S12. Origin of atomic orbitals that contribute to molecular orbital ground state and excited state for 420 nm excitation of **A**.

	Ground State Composite Orbital	Excited State Composite Orbital	Difference
Rh(I)	8.4%	15.0%	+6.6%
Rh(III)	20.8%	30.4%	+9.6%
Equatorial Cl's	53.6%	12.4%	-41.2%
Axial Cl's	11.9%	6.9%	-5.0%
dfpma	3.9%	32.7%	+28.8%
MeNC	1.4%	2.6%	+1.2%

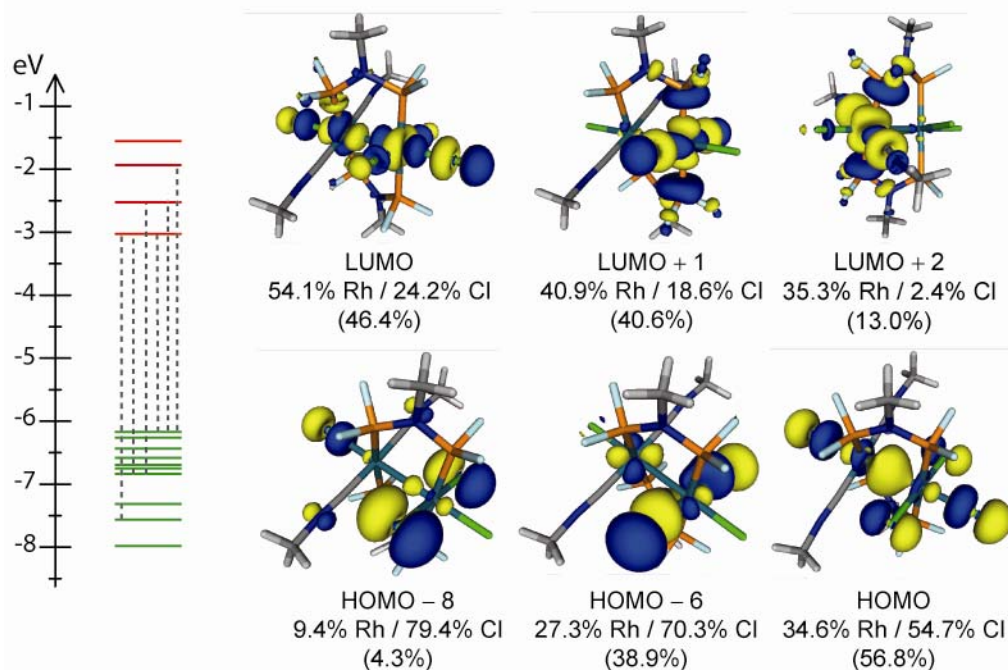


Figure S39. Excitation profile for 425 nm excitation of **A**. The molecular orbital manifold (left) is presented with filled orbitals shown in green and empty orbitals shown in red. Contributing electronic transitions to the overall excitation are noted with dashed lines. Contributing MO's to the excitation are presented (right). The percent contribution of Rh and Cl are shown directly underneath the MO label with the contribution of the MO to the total excitation presented within parenthesis.

Table S13. Origin of atomic orbitals that contribute to molecular orbital ground state and excited state for 420 nm excitation of **A**.

	Ground State Composite Orbital	Excited State Composite Orbital	Difference
Rh(I)	14.7%	17.4%	+2.7%
Rh(III)	16%	28.9%	+12.9%
Equatorial Cl's	40.8%	10.8%	-30.0%
Axial Cl's	21.0%	8.3%	-12.7%
dfpma	5.5%	31.2%	+25.7%
MeNC	2.0%	3.4%	+1.4%

H.2. Excited State Calculation of Rh₂[I,III] Structure B

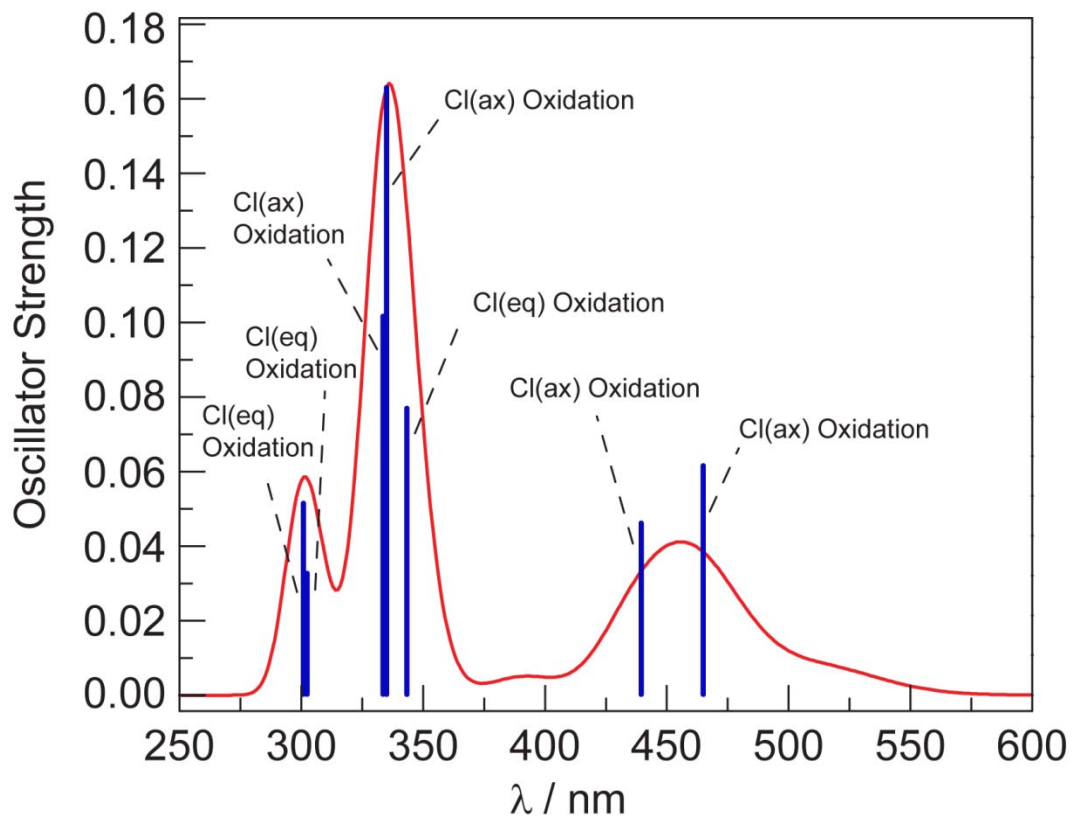


Figure S40. Relevant oscillators (solid blue bars) from TD-DFT calculations for **B** with simulated absorption spectrum overlaid (solid red line)

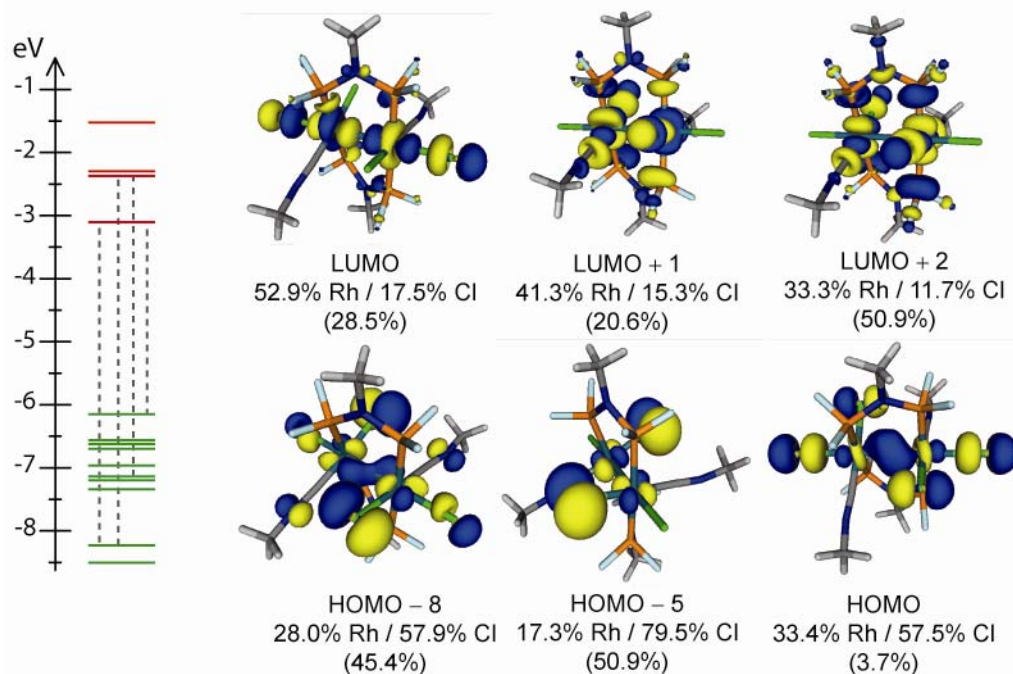


Figure S41. Excitation profile for 344 nm excitation of **B**. The molecular orbital manifold (left) is presented with filled orbitals shown in green and empty orbitals shown in red. Contributing electronic transitions to the overall excitation are noted with dashed lines. Contributing MO's to the excitation are presented (right). The percent contribution of Rh and Cl are shown directly underneath the MO label with the contribution of the MO to the total excitation presented within parenthesis.

Table S14. Origin of atomic orbitals that contribute to molecular orbital ground state and excited state for 344 nm excitation of **B**.

	Ground State Composite Orbital	Excited State Composite Orbital	Difference
Rh(II) _a	11.3%	21.2%	+9.9%
Rh(II) _b	11.4%	23.4%	+12.0%
Equatorial Cl's	61.2%	10.3%	-50.9%
Axial Cl's	7.7%	5.6%	-2.1%
dfpma	2.2%	32.8%	+30.6%
MeNC	6.2%	6.7%	+0.5%

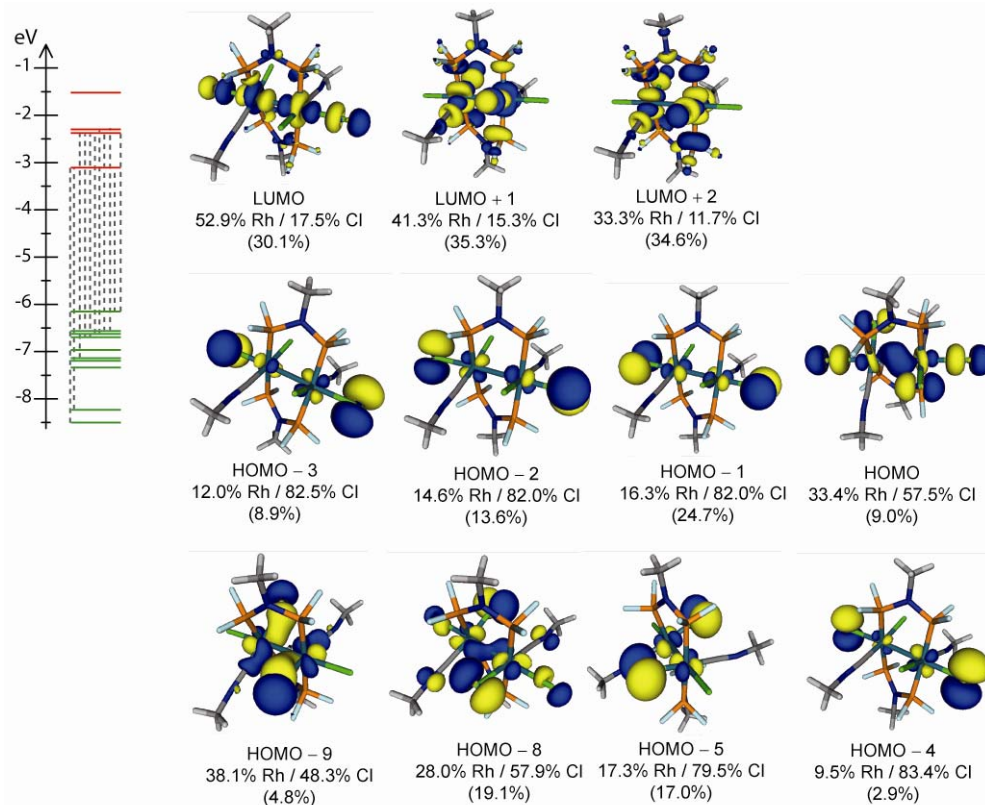


Figure S42. Excitation profile for 335 nm excitation of **B**. The molecular orbital manifold (left) is presented with filled orbitals shown in green and empty orbitals shown in red. Contributing electronic transitions to the overall excitation are noted with dashed lines. Contributing MO's to the excitation are presented (right). The percent contribution of Rh and Cl are shown directly underneath the MO label with the contribution of the MO to the total excitation presented within parenthesis.

Table S15. Origin of atomic orbitals that contribute to molecular orbital ground state and excited state for 335 nm excitation of **B**.

	Ground State Composite Orbital	Excited State Composite Orbital	Difference
Rh(II) _a	10.5%	21.1%	+10.6%
Rh(II) _b	10.0%	20.9%	+10.9%
Equatorial Cl's	27.3%	9.2%	-18.1%
Axial Cl's	45.9%	5.5%	-40.4%
dfpma	2.3%	36.1%	+33.8%
MeNC	4.0%	7.2%	+3.2%

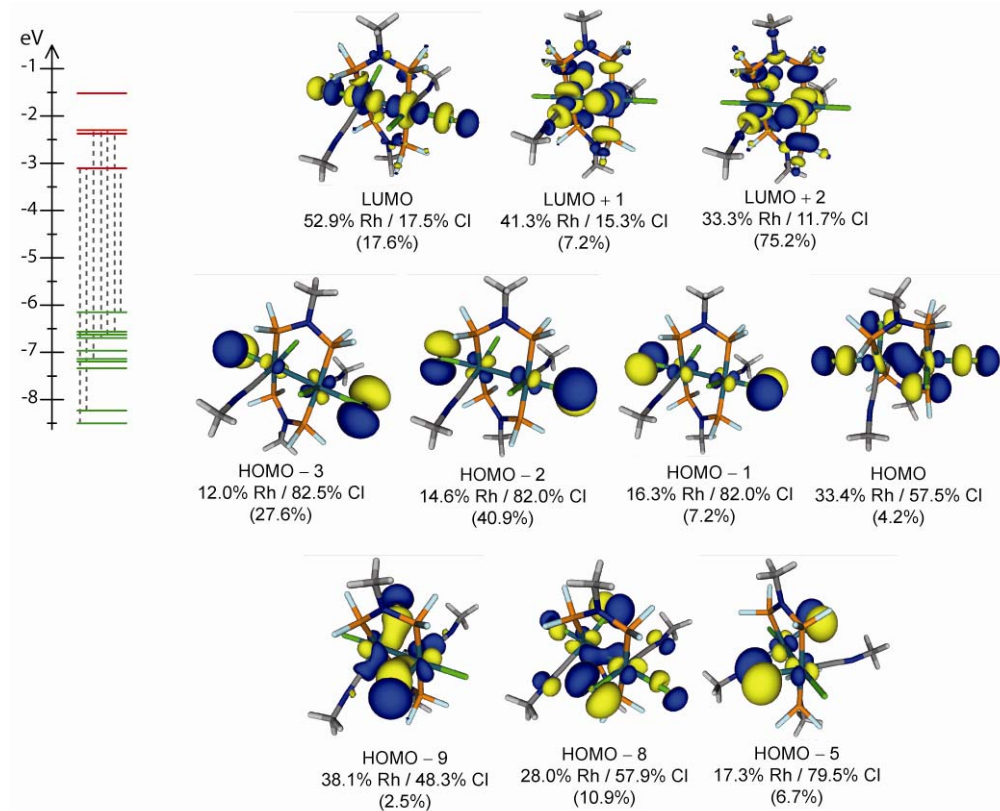


Figure S43. Excitation profile for 334 nm excitation of **B**. The molecular orbital manifold (left) is presented with filled orbitals shown in green and empty orbitals shown in red. Contributing electronic transitions to the overall excitation are noted with dashed lines. Contributing MO's to the excitation are presented (right). The percent contribution of Rh and Cl are shown directly underneath the MO label with the contribution of the MO to the total excitation presented within parenthesis.

Table S16. Origin of atomic orbitals that contribute to molecular orbital ground state and excited state for 334 nm excitation of **B**.

	Ground State Composite Orbital	Excited State Composite Orbital	Difference
Rh(II) _a	8.8%	20.0%	+11.2%
Rh(II) _b	8.2%	17.4%	+9.2%
Equatorial Cl's	13.8%	9.8%	-4.0%
Axial Cl's	63.6%	3.2%	-60.4%
dfpma	2.2%	41.0%	+38.8%
MeNC	3.4%	8.6%	+5.2%

H.3. Excited State Calculation of Chloride-Bridged Dirhodium Structure C

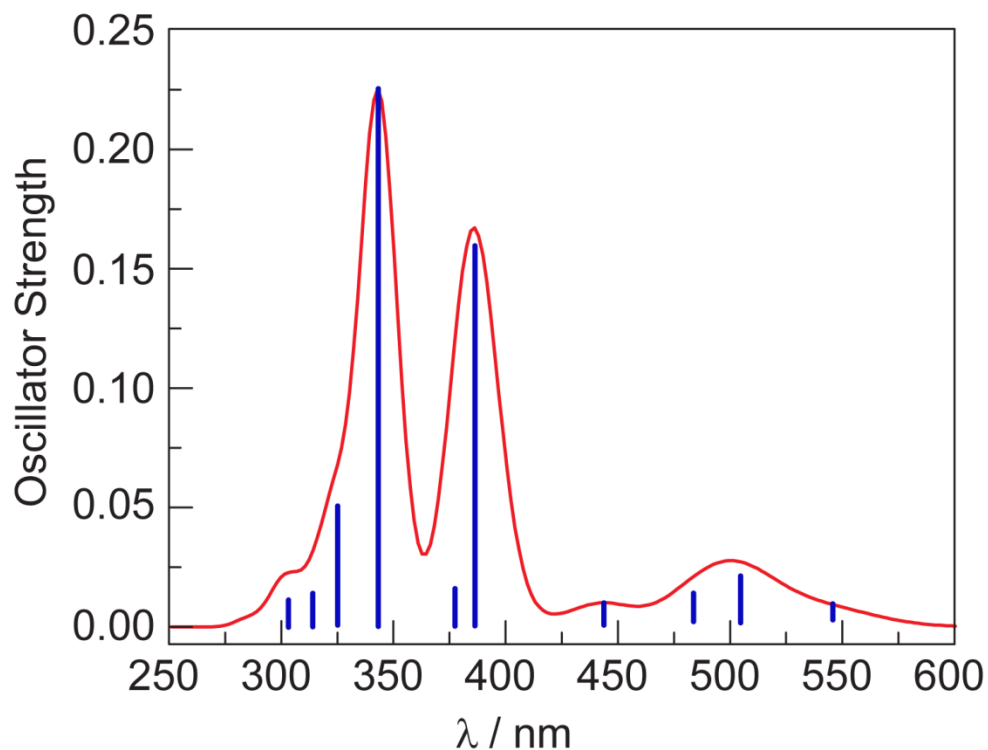


Figure S44. Relevant oscillators (solid blue bars) from TD-DFT calculations for **C** with simulated absorption spectrum overlaid (solid red line)

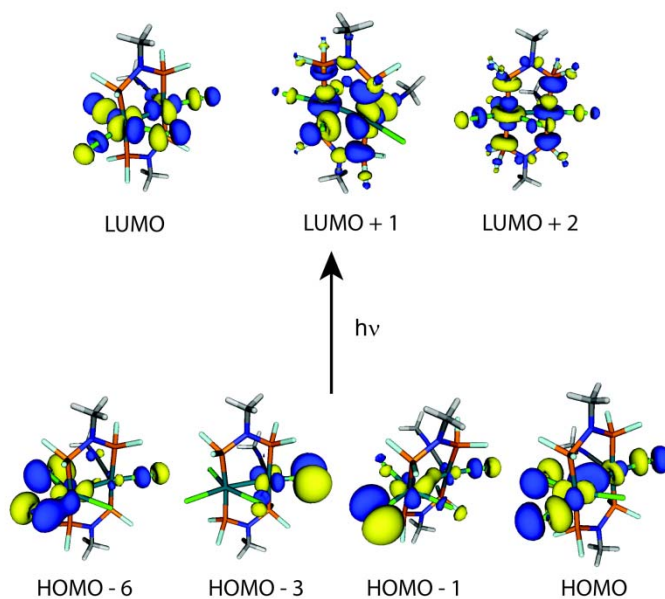


Figure S45. Primary molecular orbitals contributing to calculated electronic transitions found for **C** presented with an isovalue of 0.4.

Table S17. Composite ground state orbital contribution for major absorption feature oscillators for **C**.

Wavelength	HOMO - 6	HOMO - 3	HOMO - 1	HOMO
343 nm*	78.7%	0.0%	0.0%	12.3%
387 nm	55.6%	12.9%	15.3%	16.2%
505 nm	0.0%	0.0%	48.1%	51.9%

*9.0% contribution of HOMO-10

Table S18. Composite excited state orbital contribution for major absorption feature oscillators for **C**.

Wavelength	LUMO	LUMO + 1	LUMO + 2
343 nm	22.1%	17.8%	60.1%
387 nm	28.7%	26.7%	44.6%
505 nm	16.5%	51.6%	31.9%

H.4. Full Citation for Reference 13

Gaussian 03, Revision B.05, Frisch, M. J.; Trucks, G. W.; Schlegel, H. B.; Scuseria, G. E.; Robb, M. A.; Cheeseman, J. R.; Montgomery, Jr., J. A.; Vreven, T.; Kudin, K. N.; Burant, J. C.; Millam, J. M.; Iyengar, S. S.; Tomasi, J.; Barone, V.; Mennucci, B.; Cossi, M.; Scalmani, G.; Rega, N.; Petersson, G. A.; Nakatsuji, H.; Hada, M.; Ehara, M.; Toyota, K.; Fukuda, R.; Hasegawa, J.; Ishida, M.; Nakajima, T.; Honda, Y.; Kitao, O.; Nakai, H.; Klene, M.; Li, X.; Knox, J. E.; Hratchian, H. P.; Cross, J. B.; Bakken, V.; Adamo, C.; Jaramillo, J.; Gomperts, R.; Stratmann, R. E.; Yazyev, O.; Austin, A. J.; Cammi, R.; Pomelli, C.; Ochterski, J. W.; Ayala, P. Y.; Morokuma, K.; Voth, G. A.; Salvador, P.; Dannenberg, J. J.; Zakrzewski, V. G.; Dapprich, S.; Daniels, A. D.; Strain, M. C.; Farkas, O.; Malick, D. K.; Rabuck, A. D.; Raghavachari, K.; Foresman, J. B.; Ortiz, J. V.; Cui, Q.; Baboul, A. G.; Clifford, S.; Cioslowski, J.; Stefanov, B. B.; Liu, G.; Liashenko, A.; Piskorz, P.; Komaromi, I.; Martin, R. L.; Fox, D. J.; Keith, T.; Al-Laham, M. A.; Peng, C. Y.; Nanayakkara, A.; Challacombe, M.; Gill, P. M. W.; Johnson, B.; Chen, W.; Wong, M. W.; Gonzalez, C.; and Pople, J. A.; Gaussian, Inc., Wallingford CT, 2004.